Alternating and Gaussian Fermionic Isometric Tensor Network States

Yantao Wu,[1,*] Zhehao Dai,[2,3] Sajant Anand,[2] Sheng-Hsuan Lin,[4] Qi Yang,[1,5] Lei Wang,[1] Frank Pollmann,[4] and Michael P. Zaletel[2,6]

[1] *Institute of Physics, Chinese Academy of Sciences, Beijing 100190, China*

[2] *Department of Physics, University of California, Berkeley, California 94720, USA*

[3] *Department of Physics and Astronomy, University of Pittsburgh, Pennsylvania 15213, USA*

[4] *Department of Physics, TFK, Technische Universität München, James-Franck-Straße 1, 85748 Garching, Germany*

[5] *University of Chinese Academy of Sciences, Beijing 100049, China*

[6] *Material Science Division, Lawrence Berkeley National Laboratory, Berkeley, California 94720, USA*

(Received 28 February 2025; revised 18 June 2025; accepted 30 September 2025; published 5 November 2025)

Isometric tensor networks in two dimensions enable efficient and accurate study of quantum many-body states, yet the effect of the isometric restriction on the represented quantum states is not fully understood. We address this question in two main contributions. First, we introduce an improved variant of isometric tensor network states (isoTNS) in two dimensions, where the isometric arrows on the columns of the network alternate between pointing upward and downward; hence the name *alternating isometric tensor network states*. Second, we introduce a numerical tool—the *isometric Gaussian fermionic TNS* (isoGfTNS)—that incorporates isometric constraints into the framework of Gaussian fermionic tensor network states. We demonstrate in numerous ways that alternating isoTNSs represent many-body ground states of two-dimensional quantum systems significantly better than the original isoTNSs. First, we show that the entanglement in an isoTNS is mediated along the isometric arrows and that alternating isoTNSs mediate entanglement more efficiently than conventional isoTNSs. Second, alternating isoTNSs correspond to a deeper, and thus more representative, sequential-circuit construction of depth $\mathcal{O}(L_x \cdot L_y)$ compared to the original isoTNSs of depth $\mathcal{O}(L_x + L_y)$. Third, using the Gaussian framework and gradient-based energy minimization, we provide numerical evidence of better bond-dimension scaling and variational energy of alternating isoGfTNSs for ground states of various free-fermionic models, including the Fermi surface, the band insulator, and the $p_x + ip_y$ mean-field superconductor. Finally, benchmarking on the transverse-field Ising model, we demonstrate that an alternating isoTNS provides substantially improved performance and stability relative to the original isoTNS for the ground-state search algorithm in interacting systems.

DOI: 10.1103/8ypw-c8t4

I. INTRODUCTION

Recently, two-dimensional (2D) tensor network states (TNSs) [1–4] have become a valuable tool for studying strongly interacting quantum phases of matter [5–8]. Despite the usefulness of 2D TNSs, several outstanding research challenges remain that limit their applicability, namely reducing the complexity of contracting the tensor network to compute physical observables and improving the convergence speed in optimizing the variational tensors. For one-dimensional (1D) TNSs, i.e., matrix product states (MPSs), the isometric form is the key to the stability and efficiency of ground-state MPS algorithms such as the density matrix renormalization group (DMRG) [9,10] and time-evolution MPS algorithms based on time-evolving block decimation [11] or the time-dependent variational principle [12]. Thus, it is natural to consider the generalization of the isometric form to 2D. The most straightforward version, proposed in Ref. [13] and shown in Fig. 1(a), is known as isometric tensor network states (isoTNSs). Similar versions have also been proposed in Refs. [14,15].

In an isoTNS, each bond in the 2D network is assigned an arrow, and each tensor, when viewed as a map A from the outgoing legs to the incoming legs, is required to be an isometric linear map, $A^\dagger A = \mathbb{I}$. In particular, all physical

*Contact author: yantaow@iphy.ac.cn

Published by the American Physical Society under the terms of the Creative Commons Attribution 4.0 International license. Further distribution of this work must maintain attribution to the author(s) and the published article's title, journal citation, and DOI.

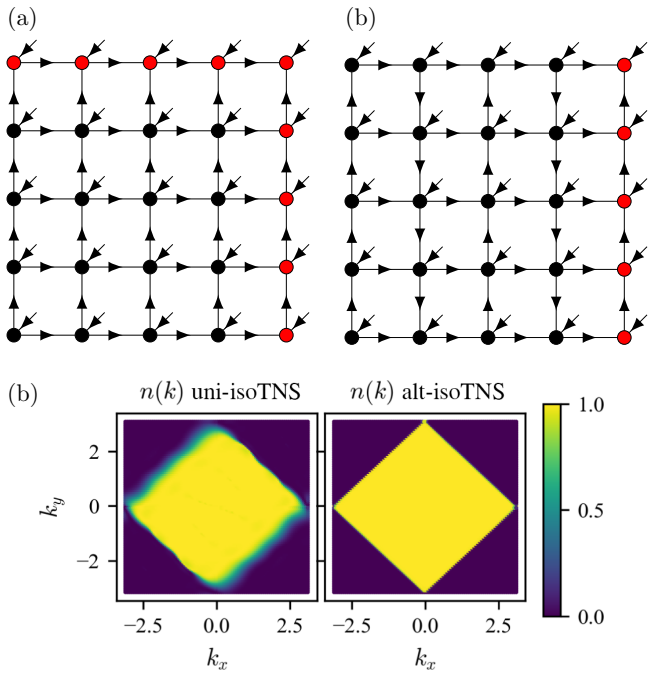


FIG. 1. (a),(b) A 5×5 (a) uniform and (b) alternating isoTNS with open boundary conditions. The orthogonality center is the single, upper right tensor with all incoming legs. The orthogonality hypersurface is the set of red tensors. Note for the alt-isoTNS that the isometry arrow direction of the columns alternates, while for uni-isoTNSs all the column arrows point up. (c) The contour plot of the k-space occupation number of the uni- (left) and alt-isoTNS (right) at bond dimension $\chi = 16$, representing the Fermi-surface ground state of Eq. (29).

legs are incoming. This allows both the efficient *exact* contraction of the norm of the 2D TNS and evaluation of expectation values of local operators on the orthogonal hypersurface [13]. In 1D, every MPS can be exactly brought into the isometric form with the same maximal bond dimension through gauge transformations. In other words, the manifolds of generic MPSs of bond dimension χ and MPSs in the isometric form of bond dimension χ are the same. In 2D, the isoTNS is a more restricted *Ansatz* than a general TNS with the same bond dimension, and the generic and isometric manifolds of dimension χ are believed to be inequivalent. How the representation power of the TNS is affected by imposing the isometric constraint is an open question.

Quantum computation provides a separate motivation for studying the representability of isoTNSs. Any 1D MPS of length L can be prepared on a quantum computer by a local sequential circuit of depth L [16]. This is not true for 2D TNS unless the network has an isometric form. Thus, it is prudent to understand the impact that isometric constraints can have on the resulting sequential circuits, especially as the representability of sequential quantum circuits has recently attracted significant interest [17–20].

Moreover, there actually exists freedom in choosing the isometric direction of the tensors while maintaining the algorithmic advantages and sequential-circuit representations. For examples, see Figs. 1(a) and 1(b), where we show the networks of primary interest in this work. This network design choice has not been explored in previous isoTNS works [13,21–24]. However, this turns out *not* to be a gauge degree of freedom and can significantly affect the representability of the TNS *Ansatz* and the sequential circuit. To understand the effect of different isometric forms, we provide insight from two perspectives—entanglement structure and the corresponding sequential quantum circuits—and support this with numerical evidence of representing ground states of both noninteracting fermionic and interacting spin systems.

In this paper, we show that in an isoTNS, entanglement is, in a sense made precise later, mediated *along* the isometric arrows. An isoTNS is capable of representing almost any short-ranged correlated state, but it can be inefficient in capturing entanglement *perpendicular* to its isometric directions. This severely limits the application of isoTNSs to some of the most important physical systems such as Fermi liquids. Here, we propose a novel isometric *Ansatz*, the alternating isoTNS (alt-isoTNS), shown in Fig. 1(b), which greatly improves the representability of isoTNSs while keeping all algorithmic advantages over general TNSs. To differentiate from the alt-isoTNS, hereafter, we call the original isoTNS [13], shown in Fig. 1(a), the uniform isoTNS (uni-isoTNS).

Another independent contribution of this paper is to introduce a tool to efficiently study the representability of isoTNSs—isometric Gaussian fermionic tensor network states (isoGfTNSs). The isoGfTNS is a variational *Ansatz* resulting from imposing an isometric constraint on the Gaussian fermionic tensor network states (GfTNSs). The general problem of 2D TNS representability can be very difficult to study due to high computational complexity in optimizing a generic, interacting 2D TNS. However, analysis can be performed by imposing the Gaussian constraint on the variational *Ansatz*, which simplifies the calculation, and by choosing free-fermion systems as a benchmark problem, where the exact solution exists [25]. Since the key quantity restricting the TNS representability is the entanglement, free fermions, which can be highly entangled while still exactly solvable, are good nontrivial benchmark problems to test TNS representability in a controlled setting. In fact, significant understanding of TNS representability has been gained within the GfTNS formalism, with recent studies focusing on chiral states [26,27], d-wave superconductivity [28], and the Fermi surface [29]. A related discussion on frustration-free free fermions has also recently appeared [30].

In this paper, we explain how the isometric property can be enforced as a additional constraint on top of Gaussianity within the GfTNS formalism and provide a

gradient-based numerical algorithm for finding the ground state of free-fermion Hamiltonians with isoGfTNSs. We use this global-optimization algorithm to assess the representability of alt-isoTNSs versus uni-isoTNSs, free from the pitfalls of local optimization methods used for interacting quantum systems. Using the isoGfTNS algorithm, we show that the alt-isoTNS clearly captures the Fermi surface of a free-fermion metal on a square lattice significantly better than the uni-isoTNS. As seen in Fig. 1(c), the Fermi surface found by the alt-isoTNS is demonstrably sharper and more symmetric.

Despite the focus of this work on developing new classical numerical methods, we would like to highlight its origin and impact on quantum information. Due to the equivalence of isoTNSs and sequential quantum circuits [18,31], the two main contributions of the paper have the following implications on the study of sequential quantum circuits.

(i) *Gaussian fermion isoTNSs*. The newly proposed isoGfTNS framework provides an efficient tool to study the representability of sequential quantum circuits for many-body quantum systems, particularly the effect of circuit geometry on the circuit representability.
(ii) *Alt-isoTNSs*. The better representability of alt-isoTNSs over uni-isoTNSs indicates that the resulting sequential quantum circuit layout outperforms the original sequential quantum circuit.

Given a fixed number of gates, the new geometry improves the accuracy of low-energy quantum state preparation, which is the crucial building block for many quantum applications, such as the determination of spectral functions through quenches and ground-state energies via quantum phase estimation. In fact, the correspondence to sequential quantum circuits has originally motivated this work. Through the lens of quantum circuits, we ask the question, what happens if we construct an isoTNS *Ansatz* with different quantum circuit-depth scaling? This, then, leads to our new *Ansatz*, which significantly improves the representability of the isoTNS *Ansatz* for strongly entangled many-body ground states [cf. Fig. 1(c)] and the stability of the classical ground-state algorithm [cf. Fig. 15].

The ability of isoTNSs to be efficiently optimized classically and prepared on quantum devices makes it a strong candidate for quantum tasks that require efficiently obtainable classical inputs. Quantum quenches are one such example, where the ground state is first obtained classically, and then prepared on a quantum computer for subsequent dynamics—a task at which quantum computers excel. In this context, the isoGfTNS is also useful beyond free (Gaussian-fermionic) systems, particularly when the subsequent dynamics is interacting (non-Gaussian).

This paper is organized as follows. In Sec. II, we introduce the alt-isoTNS and explain how it mediates entanglement differently than the uni-isoTNS. We then discuss the difference between the alt-isoTNS and the uni-isoTNS in terms of sequential quantum circuits and holographic state preparation. We next demonstrate that all quantum double fixed points have exact alt-isoTNS representations. The section ends with a discussion on how the usual uni-isoTNS algorithms for interacting quantum systems can be easily modified for the alt-isoTNS *Ansatz*. In Sec. III, we introduce the isoGfTNS framework and the necessary optimization algorithms. This section is of independent interest from alt-isoTNSs, as we can consider arbitrary, consistent isomeric conditions and explore the representability of different isoTNSs within this framework. In Sec. IV, we first study noninteracting models, including the 2D Fermi surface and gapped free-fermion insulators, providing numerical evidence of the superior representation of the alt-isoGfTNS compared to the uni-isoGfTNS. We next perform a study of the interacting 2D transverse-field Ising model where the alt-isoTNS demonstrates significantly better performance and algorithmic stability than the uni-isoTNS in finding the ground state. Finally, in Sec. V, we discuss future directions for isometric tensor networks and conclude.

II. ALTERNATING ISOMETRIC TENSOR NETWORK STATES

Isometric tensor network states are tensor network states where each tensor satisfies certain isometric constraints. In 1D, there are two natural choices for isometric constraints, often referred to as left-canonical form and right-canonical form. A tensor $A_{p,l,r}$ is called left-canonical if $\sum_{p,l} A_{p,l,r}A^*_{p,l,r'} = \delta_{r,r'}$, where p, l, and r are, respectively, the physical, left, and right index of the tensor. Correspondingly, a right-canonical tensor satisfies $\sum_{p,r} A_{p,l,r}A^*_{p,l',r} = \delta_{l,l'}$. It is convenient to represent this isometric condition graphically in terms of the arrows. The arrows indicate how legs of the tensors, i.e., indices, should be grouped so that the resulting matrix is an isometry; in our convention, the matrix A with all incoming and outgoing legs forming the row and column indices, respectively, is isometric; $A^\dagger A = \mathbb{I}$. Below, we refer to the arrow direction as the isometric direction.

In 1D, any matrix product state can be written in a left-canonical (or right-canonical) form with the same bond dimension. In 2D, there is a nontrivial freedom of choice in the isometric directions of the tensors that has been unexplored up until now. Unlike in the 1D case, 2D isoTNSs form a strict subset of 2D TNSs, and different choices of isometric directions give different subsets of general TNSs. In a conventional uni-isoTNS, the isometric arrows of each isometry [the black tensors in Fig. 1(a)] all point toward the same direction, e.g., the upper right in Fig. 1(a). In an

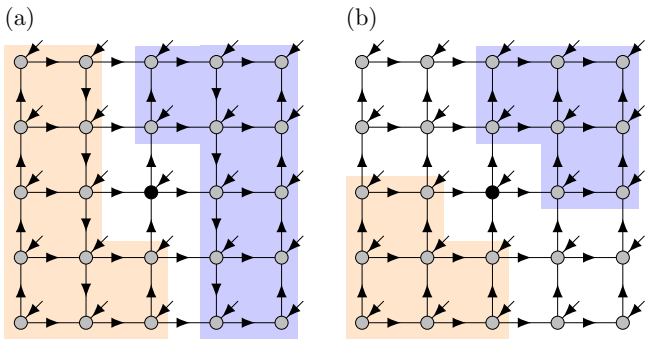


FIG. 2. The causal structure of (a) the uni-isoTNS and (b) the alt-isoTNS. For the single-site tensor colored in black, its future (past) light cone is colored in orange (blue). The uncolored tensors belong to the spacelike region outside the light cone.

alt-isoTNS, we keep the horizontal isometric arrows pointing rightward but alternate the vertical isometric arrows between upward and downward pointing on even and odd columns. With open boundary conditions, there exists an orthogonality hypersurface (OHS) of tensors, which only has arrows point inward, depicted in red in Fig. 1. The OHS is composed of a column and a row in an uni-isoTNS, while it is only composed of a column in an alt-isoTNS. The OHS can be treated as an MPS embedded in the 2D network, and the orthogonality center (OC) is the single tensor with all incoming legs. As will be shown, the alt-isoTNS retains all the algorithmic efficiencies that enable efficient classical manipulation and optimization of the uni-isoTNS but greatly improves wave-function representability.

A first hint of the physical difference resulting from the isometric structure is in the causal light cones shown in Fig. 2. Here, we define the *future light cone* of a tensor as the sites where the on-site expectation values of the physical observables are affected by the change of the tensor (shown in black). The future light cone, highlighted in orange, of a tensor includes all tensors that can be reached by going *against* the flow of arrows on the legs. The *past light cone*, highlighted in blue, is the set of tensors that can affect the on-site expectation values of physical observables of the current (black) tensor, reached by going *with* the flow of arrows. A tensor is *spacelike* separated from the black tensor if it is neither in the causal past nor the future of the black tensor. In alt-isoTNSs no tensors are spacelike separated from the black tensor, while in uni-isoTNSs there exist two regions of spacelike separation from the black tensor. This light-cone structure follows from the isometric structure and has a direct impact on both the entanglement structure and the sequential quantum circuit construction.

A. Mediating entanglement along diagonals

We next discuss the marked differences in entanglement structure between uni-isoTNSs and alt-isoTNSs, focusing on the isometric structures shown in Figs. 1(a) and 1(b). A uni-isoTNS prefers to entangle physical sites along the $(1,1)$ diagonal, which aligns with its light cone. An alt-isoTNS, on the other hand, does not have this anisotropy. To make this anisotropy manifestly clear, consider a concrete, albeit manufactured, example state $|\diagup\rangle$, which is an $L_x \times L_y$ 2D state formed from the tensor product of $L_x + L_y$ decoupled chains along the $(1,1)$ diagonals, and contrast it with the state $|\diagdown\rangle$, the analogous state formed by a tensor product of $L_x + L_y$ decoupled chains along the $(1,-1)$ direction. For simplicity, we assume that each decoupled chain is an 1D area-law state and thus can be efficiently represented by an MPS with a finite bond dimension χ.

Since both $|\diagup\rangle$ and $|\diagdown\rangle$ are tensor products of 1D states, we can utilize the MPS representation of the 1D states to construct the 2D isoTNS representation. For an uni-isoTNS, we can represent $|\diagup\rangle$ efficiently by embedding the MPS representation of each chain directly into the 2D state. We show the MPS representation in isometric form for two $(1,1)$ chains, e.g., the blue and the orange MPS, in Fig. 3(a). Such representations can be efficiently embedded as part of a uni-isoTNS while remaining consistent with

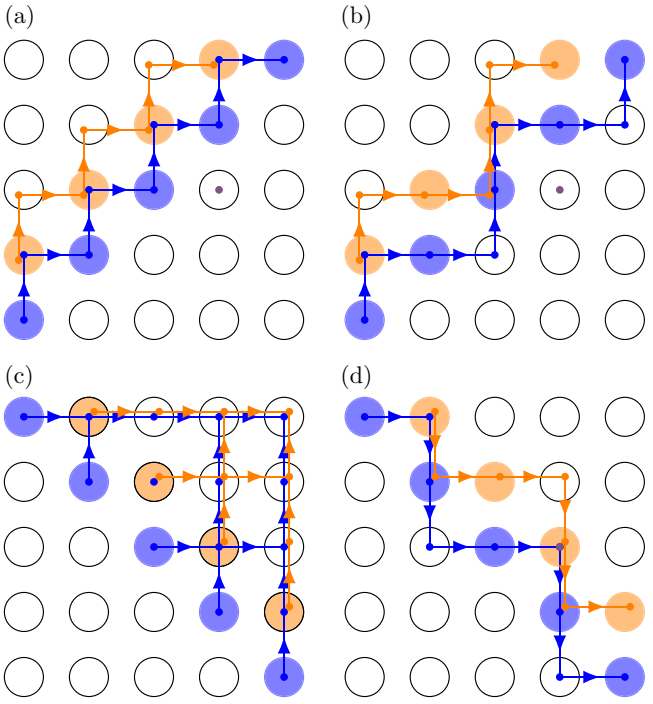


FIG. 3. The (a),(c) uni-isoTNS and (b),(d) alt-isoTNS representations of decoupled chains (a),(b) along the $(1,1)$ diagonals and (c),(d) along the $(1,-1)$ diagonals. Two chains, one in blue and one in orange, are shown. The physical indices are suppressed for visual clarity. Crucially, the uni-isoTNS representation of $|\diagdown\rangle$ requires a multiscale entanglement renormalization *Ansatz* (MERA) structure, while the alt-isoTNS representation mediates all entanglement locally.

the isometric (arrow) direction. A different construction for $|\diagup\rangle$ is given for the alt-isoTNS in Fig. 3(b). Due to the isometric constraint on the columns, we can only pass the information upward at specific columns. As a result, the uni-isoTNS is slightly more efficient than the alt-isoTNS in mediating the entanglement along the $(1,1)$ direction: the uni-isoTNS requires bond dimension χ for each bond while the alt-isoTNS requires bond dimension χ^2 when two MPS embeddings overlap.

A drastic difference shows up when we consider the case of the $|\diagdown\rangle$ state. For an alt-isoTNS, we can again represent $|\diagdown\rangle$ efficiently by embedding the MPS representation of each chain directly into the 2D state. We show the MPS representation in isometric form for $(1,-1)$ chains, e.g., the blue and the orange MPS in Fig. 3(d). Similarly to the construction for $|\diagup\rangle$, we can only pass the information downward at specific columns, and therefore we require a bond dimension of χ^2, independent of system size L. However, the physical sites along a coupled $(1,-1)$-diagonal chain are spacelike separated in uni-isoTNSs. Due to the lack of downward-pointing isometry arrows, the only way to encode nontrivial correlations between two sites is to encode the information in a tensor in the common causal past. This requirement is particularly bad for the *exact* representation of decoupled chains on an *system with open boundary condition*. For the five-site (blue) and four-site (orange) chains shown in Fig. 3(c), only the single tensor in the top-right corner can mediate the entanglement between the two ends of the chains. For an $L \times L$ system with open boundary conditions, we need at least a bond dimension 2^{L-1} at the top-right corner to exactly represent the $|\diagdown\rangle$ state.

The requirement of the enormous bond dimension at the corner for uni-isoTNSs can be significantly alleviated if we consider a periodic tensor network or allow minor errors in the representation. To better compare the average bond dimension of approximate uni-isoTNS and alt-isoTNS representations, we consider the case where each decoupled chain in the $|\diagdown\rangle$ state is a near-critical state with a long correlation length ξ; the nearby critical point is assumed to be described by a conformal field theory with a central charge c. According to Ref. [32], the MPS representing this state has a bond dimension $\chi \sim \xi^{1/\kappa}$, where κ is a function of the central charge. Similar to Fig 3(d), each diagonal chain uses $2L$ bonds on a $L \times L$ periodic alt-isoTNS; the product of all bond dimensions for a single chain is χ^{2L}. Stacking all chains, the *geometric average* of the $2L^2$ bond dimensions is $\chi_{\text{alt}} = \chi^{2L\times L/2L^2} = \chi$. For the uni-isoTNS, an efficient way to represent the diagonal chain while respecting the isometric structure is to embed a multiscale entanglement renormalization *Ansatz* (MERA) into the isoTNS. As shown in Fig. 3(c), the disentangling direction of the MERA corresponds to the $(1,1)$ direction of the isoTNS; they have consistent isometric arrows. We estimate the bond dimension of the MERA to be $\exp(c/6)$ [33] and the depth of the MERA to be $O(\ln(\xi))$. At level d of the MERA, we have $L/2^d$ sites left, but the distance between neighbors becomes 2^d; therefore, the embedding uses $2L$ bonds at each level. This counting leads to a geometric average of bond dimensions $\chi_{\text{uni}} \sim e^{(c/6)O(\ln(\xi))} \sim \chi_{\text{alt}}^{\eta}$. Determining the exact value of η is difficult due to $O(1)$ uncertainties in the estimation. Since we can collapse each MERA into an MPS without changing the product of the bond dimensions, η must be greater than or equal to 1. In Sec. III, we introduce the Gaussian fermion isoTNS and apply it in Sec. IV A to numerically test the argument presented here. Our numerical results suggest that $\eta > 1$. Unlike the naive argument, η is independent of system size.

In conclusion, the alt-isoTNS behaves the same for decoupled chains in the $(1,1)$ direction and decoupled chains in the $(1,-1)$ direction. We expect the uni-isoTNS to have an advantage over the alt-isoTNS for mediating entanglement in the $(1,1)$ direction but a disadvantage for the $(1,-1)$ direction. For an isotropic system, there are entangled degrees of freedom with arbitrary separations, and we expect the dominant error to come from the worst direction. Since the alt-isoTNS is more symmetric in mediating entanglement, we expect it to be an overall better *Ansatz*. In Sec. IV E, we show numerical evidence supporting this argument for interacting, isotropic spin models.

B. Sequential quantum circuits

Beyond their utility for numerical and analytical studies, isometric tensor networks have a direct correspondence to sequential quantum circuits and provide concrete unitary circuits for qubit-efficient state preparation on quantum computers [16,31,34–36]. This has been demonstrated experimentally in 1D for both MPSs [37] and entanglement renormalization tensor networks [38,39] and explored numerically in 2D [40].

To recap the general principle behind mapping isometric tensor networks to quantum circuits, consider an MPS in right-canonical form (left-pointing isometry arrows) with bond dimension χ and physical Hilbert-space dimension $d = 2$, as shown in Fig. 4. Starting from the left end, the

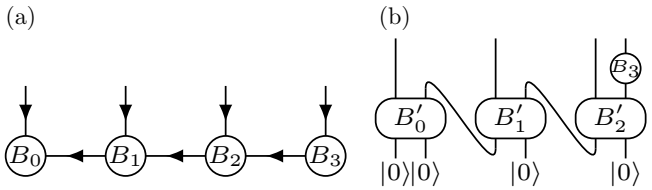


FIG. 4. The sequential-circuit representation of an isometric MPS. B_i' is a unitary matrix obtained from adding orthogonal columns to the isometric matrix B_i. (a) The right-canonical MPS. (b) The sequential circuit.

first isometric tensor can be expanded into a unitary acting on a physical qubit initialized to some fixed state, typically $|0\rangle \in \mathbb{C}^2$ and a bond qudit of dimension χ, typically also initialized to $|0\rangle \in \mathbb{C}^\chi$; the bond qudit can also be viewed as a register of $\log_2(\chi)$ qubits. The isometry is expanded into a unitary by adding orthogonal columns that dictate the action of the gate when the physical qubit is in any state orthogonal to the desired one, e.g., $|1\rangle$. The unitary derived from the tensor on the second site acts on a fresh physical qubit in $|0\rangle$ and the bond qubit from the first site, which carries correlations from site to site. In this way, a length-L MPS can be sequentially prepared by a depth-L circuit, nominally using L qubits [16].

This idea directly carries over to all isometric tensor networks and in particular to the 2D geometries depicted in Fig. 1. A bond dimension χ uni-isoTNS corresponds to a depth $\mathcal{O}(L_x + L_y)$ state-preparation circuit; e.g., the 3×3 uni-isoTNS shown in Fig. 5(a) corresponds to a depth-5 circuit preparing the nine-qubit state. At each time step t, the unitary gates corresponding to the tensors a Manhattan distance t from the OC (upper right) can be applied in parallel. Once again, the light-cone picture plays an important role here. Gates with spacelike separation can be applied simultaneously. Additionally, the notion of past and future causal cones indicates which gates in the circuit can affect physical observables on sites and thus affect the pattern of entanglement generated. A circuit diagram for the resulting sequential quantum circuit is shown in Fig. 5(c).

The alt-isoTNS corresponds to a drastically different circuit, as due to the alternating isometry conditions in the columns, typically only one unitary gate can be applied at each time step [41]. As an example, consider the 3×3 alt-isoTNS in Fig. 5(b) and the resulting sequential quantum circuit in Fig. 5(d). One sequentially acts all of the unitaries in the orthogonality column [down the rightmost column in Fig. 5(b)] and then crosses over into the next column, sequentially applying gates against the direction of the isometry arrows (up the middle column in Fig. 5), and so on in a snakelike pattern for the remaining columns. Thus, the alt-isoTNS corresponds to a depth $\mathcal{O}(L_x \cdot L_y)$ circuit. This corresponds to the lack of spacelike separation in the alt-isoTNS, so each tensor lies in either the future or past causal cone of each other. The quadratically deeper circuit nature of the alt-isoTNS compared to the uni-isoTNS could potentially lead to increased representability, i.e., numerical performance when optimized classically, of the alternating *Ansatz*.

The sequential quantum circuits discussed above can be combined with the holographic approach, where one prepares a D-dimensional quantum state using a number of qubits proportional to a $(D-1)$-dimensional cross section of the state [37,42]. Roughly speaking, if all we are interested in is measuring physical expectation values and not preparing the quantum state itself for further manipulation, we can recycle qubits produced from the application of the unitary by measuring the physical qubit and reusing it for the next unitary, after reinitializing it to $|0\rangle$. This can drastically decrease the required number of physical qubits to actually perform quantum simulation, at the expense of requiring midcircuit measurement and reset. In terms of sequential circuits of MPSs, expectation values can be estimated using $1 + \log_2(\chi)$ qubits, 1 for the physical qudit and the remaining ones to represent the bond qudit. For sequential circuits of uni-isoTNSs and alt-isoTNSs, $\mathcal{O}((L_x + L_y)\log_2(\chi))$ qubits and $\mathcal{O}(\min(L_x, L_y) \cdot \log_2(\chi))$ qubits are needed, respectively, for holographic simulation.

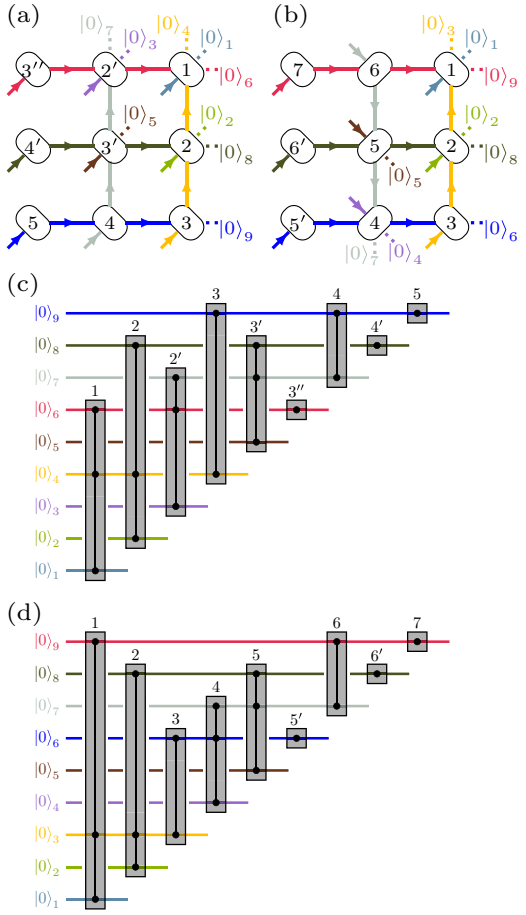


FIG. 5. (a),(b) The (a) uni-isoTNS and (b) alt-isoTNS when viewed as sequential quantum circuits to prepare a nine-qubit state. All bond dimensions are $\chi = 2$, so each line represents a qubit. Different qubits are drawn in different colors. The label of the tensors corresponds to the time step when the gate can be applied. Dotted lines indicate input qubits in the state $|0\rangle$. Due to isometry conditions on each tensor, the vertical bond dimension in the leftmost column is $\chi = 1$. (c),(d) Quantum circuit diagrams for (c) the uni-isoTNS and (d) the alt-isoTNS, where isometric tensors have been expanded into unitary gates acting on up to three qubits by adding orthogonal columns. Gates act on the qubits that continue through the rectangle. Gates with the same number act on disjoint sets of qubits and thus can be applied simultaneously.

While the uni-isoTNS requires more qubits, the depth of the resulting circuit is shorter, so the choice of better *Ansatz* in practice will depend on noise levels and qubit numbers on the particular device [38]. In particular, we expect the uni-isoTNS to be more noise resilient, as the smaller causal cones limit the negative effects that errors in gates can have on future expectation values.

We conclude by noting that prior studies have been restricted to much smaller system sizes [43–47], and that sequential circuits in the literature have focused only on uniform structures [18,31]. In addition, recent theoretical works address different but complementary aspects [48,49]. By working at larger scales, introducing alternating sequential structures, and demonstrating practical optimization schemes (Sec. IV), our results extend the understanding of sequential circuits and highlight their relevance for both quantum simulation and quantum algorithm design.

C. Topological phases

We now demonstrate a simple proof that alt-isoTNSs can represent a large class of topological orders in 2D. It has been proven that all string-net states, which contain all nonchiral topological orders with gappable edges in two dimensions [50,51], can be exactly represented as finite bond dimension uni-isoTNSs in the thermodynamic limit [52]. This construction, however, is quite complicated. Here, we present a much simpler construction for a large subset of string-net states, the quantum double states of finite group G [53], for both the uni-isoTNS and the alt-isoTNS, demonstrating the versatile representability of the alt-isoTNS. Up to normalization, local unitaries, and coarse-graining, the exact tensor in the TNS representing the ground state of the quantum double for group G is found [54] to be

$$A^{p_1p_2p_3p_4}_{lrdu} = \sum_{g\in G} g_{lp_1} g_{up_4} g^{-1}_{p_2r} g^{-1}_{p_3d}, \tag{1}$$

where g denotes both the group element and its left-regular matrix representation which is a real permutation matrix [55]. The tensor legs label group elements of G, so the bond dimension is the order of the group, $|G|$. Due to coarse-graining, $p_1p_2p_3p_4$ are grouped into one physical leg on each tensor. If one contracts any two of the virtual legs, e.g., l and d, and the physical leg of A with that of $A^\dagger$, one obtains

$$\sum_{ldp_1p_2p_3p_4} A^{p_1p_2p_3p_4}_{lrdu} A^{p_1p_2p_3p_4}_{lr'du'} \tag{2}$$

$$= \sum_{h,g\in G} \mathrm{Tr}(gh^{-1})(gh^{-1})_{uu'}(gh^{-1})_{rr'}\mathrm{Tr}(g^{-1}h) \tag{3}$$

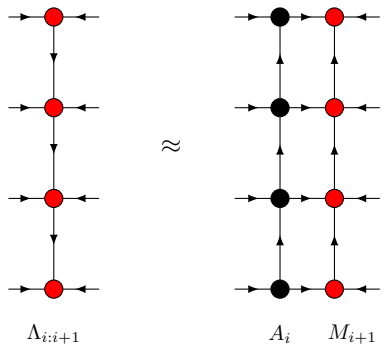
$$\propto \delta_{uu'}\delta_{rr'}, \tag{4}$$

where we have noted that because $g^{-1}h$ is again a matrix in the left-regular representation, it is traceless unless $g^{-1}h$ is the identity. This computation holds for any two virtual legs. The quantum double TNS is thus automatically both a uni-isoTNS and an alt-isoTNS. Note that the quantum double tensors actually satisfy far stronger isometric constraints than either those of uni- or alt-isoTNSs, as any grouping of two virtual legs and the physical legs leads to a valid isometry.

D. Algorithmic modification for alternating isometric tensor network states

The alt-isoTNS *Ansatz* introduced above can be implemented easily using the standard isoTNS toolbox [13,21–23] with minor modification. Crucially, the computational complexity remains the same for the time-evolution algorithm [13,22], $\mathcal{O}(\chi^7)$ and ground-state search algorithms [21], $\mathcal{O}(\chi^{10})$.

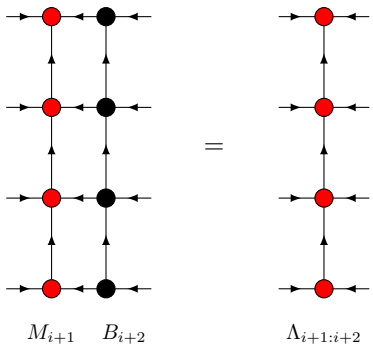
There are two key subroutines in isoTNS algorithms. One is the splitting of the orthogonality two-column $\Lambda_{i:i+1}$, analogous to the two-site wave function in an MPS, into a left-isometry column A_i and an orthogonality column M_{i+1}, analogous to an isometric tensor and normalized tensor in an MPS; this is shown diagrammatically in Eq. (5). $\Lambda_{i:i+1}$ carries the physical legs of columns i and $i+1$, with the physical legs on column i merged with the left virtual legs of $\Lambda_{i:i+1}$ and those on column $i+1$ with the right virtual legs. In the *Moses move (MM)* algorithm used to perform this splitting [13], the resulting vertical isometric arrows in A_i and M_{i+1} are always reversed from the original vertical arrows in $\Lambda_{i:i+1}$:



(5)

The vertical arrow direction in $\Lambda_{i:i+1}$ can be efficiently and exactly reversed similarly to changing the isometric form of an MPS. Thus, we can control the resulting isometric directions in A_i and M_{i+1} by choosing the corresponding opposite direction on $\Lambda_{i:i+1}$ as the input to the splitting algorithm. Explicitly, when sweeping between the columns using the MM, we can impose the alt-isoTNS (uni-isoTNS) structure by ensuring that $\Lambda_{i:i+1}$ has the same (opposite) vertical isometry direction as the previous isometric columns.

The second key subroutine in the isoTNS algorithm is the reverse of the splitting operator described above, i.e., the merging of the orthogonality column M_{i+1} and a right-isometric column B_{i+2} into a new orthogonality two-column $\Lambda_{i+1:i+2}$:



(6)

Here, for algorithmic efficiency reasons, it is advantageous if the vertical arrows on M_{i+1} and B_{i+2} have the same direction so that the resulting $\Lambda_{i+1:i+2}$ has a definite isometric form. If M_{i+1} and B_{i+2} have opposite vertical arrow directions, the direction on M_{i+1} can be reversed to agree with B_{i+2} before merging.

Thus, regardless of the desired pattern of the direction of the vertical isometry arrows, it can be achieved by reversing of the isometric form on the orthogonality columns or two columns when needed. This has a computational complexity $O(\eta^3\chi^2)$, compared to the $O(\eta^3\chi^4)$ of splitting algorithm, where η is the vertical bond dimension on the orthogonality column and χ is the bond dimension elsewhere. The cost of imposing a particular isometry structure is subleading, and thus the alt-isoTNS is, at leading order, no more computationally expensive than the uni-isoTNS.

These subroutines are used in both ground-state and time-evolution algorithms. In particular, they are used for computing local observables in an isoTNS. Any operator supported on column i and $i+1$ can be measured by applying MPS methods to $\Lambda_{i:i+1}$ after $\Lambda_{i:i+1}$ has been made into the OHS via the MM algorithm.

In Sec. IV E we investigate the performance of the uni- and alt-isoTNS in representing the ground state of the 2D transverse-field Ising model.

III. ISOMETRIC GAUSSIAN FERMIONIC TENSOR NETWORK STATES

A separate result of this paper is the introduction of a Gaussian version of the isoTNS, alternating, uniform, or otherwise. We will show how to incorporate the isometric constraint into the GfTNS framework, resulting in the isoGfTNS. As an application, this will be used to assess the representability of the alt-isoTNS versus the uni-isoTNS. It is common to optimize translationally invariant GfTNSs with a variational global approach using gradient descent to study the representation power of the *Ansatz*. In the isoGfTNS framework, the uniform and alternating constraints can be implemented by choosing the corresponding fixed isometric form in the tensor initialization. In the next section, using these techniques, we consider various noninteracting (free-)fermion models and compare the performance of uniform and alternating isoGfTNSs in representing their ground states. This allows us to investigate the effect of isometric constraints on representability with a different angle from interacting isoTNSs.

A. Fermionic Gaussian states

Let us consider a free-fermion system on a 2D square lattice of size $L_x \times L_y$, where each site hosts a complex fermion mode c. The information of a fermionic Gaussian state ρ is entirely encapsulated in its covariance matrix:

$$\Gamma^{\mu\nu}_{\mathbf{x},\mathbf{x}'} \equiv \frac{i}{2}\mathrm{Tr}(\rho[\gamma^{\mu}_{\mathbf{x}}, \gamma^{\nu}_{\mathbf{x}'}]), \tag{7}$$

where $\gamma^{\mu}_{\mathbf{x}}$ is the (real) Majorana fermion mode on site $\mathbf{x}$:

$$\gamma^{1}_{\mathbf{x}} = c^{\dagger}_{\mathbf{x}} + c_{\mathbf{x}}, \quad \gamma^{2}_{\mathbf{x}} = -i(c^{\dagger}_{\mathbf{x}} - c_{\mathbf{x}}). \tag{8}$$

In the following discussion, we consider free-fermion models with translational invariance without unit cells. The generalization to unit cells is straightforward, but the notation is onerous. We discuss unit cells in Appendix A 1. After a Fourier transform, the covariance matrix in the momentum space is

$$\Gamma^{\mu\nu}(\mathbf{k}) \equiv \frac{i}{2}\mathrm{Tr}(\rho[\gamma^{\mu}_{\mathbf{k}}, \gamma^{\nu\dagger}_{\mathbf{k}}]) = \frac{i}{2}\mathrm{Tr}(\rho[\gamma^{\mu}_{\mathbf{k}}, \gamma^{\nu}_{-\mathbf{k}}]), \tag{9}$$

where $\gamma^{\mu}(\mathbf{k}) = 1/\sqrt{L_x L_y}\sum_{\mathbf{x}} e^{-i\mathbf{k}\cdot\mathbf{x}}\gamma^{\mu}(\mathbf{x})$ with $\mu = 1$ or 2. We will adopt antiperiodic boundary conditions along the x direction, and periodic boundary conditions along the y direction to avoid parity-invariant k-points in the study of the GfTNS, following previous work [29]. Thus, $\mathbf{k} = (k_x, k_y)$ with $k_x = 2\pi(n_x + \frac{1}{2})/L_x$ and $k_y = 2\pi n_y/L_y$, for $n_i = 1, 2, \ldots, L_i$, where L_i is the number of sites along direction $i = x$ or y.

B. Gaussian fermionic tensor network states

We first review the construction of a generic *fermionic* TNS before specializing to Gaussian states. To construct a fermion TNS [25], one first prepares n_v Majorana Bell pairs over each bond of the lattice, which make up the virtual state:

$$\rho_{\mathrm{virtual}} = \prod_{b\in\mathrm{bonds}}\prod_{j=1}^{n_v}\frac{1}{2}(1 + i\gamma^{j}_{b_1}\gamma^{j}_{b_2}), \tag{10}$$

where $\gamma^{j}_{b_1}$ and $\gamma^{j}_{b_2}$ are, respectively, the jth Majorana modes on the two sites connected by bond b. Then, at each

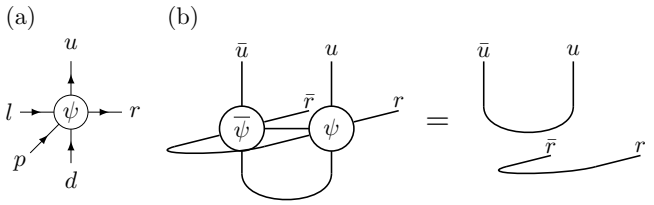


FIG. 6. (a) The isometric tensor that makes up the TNS. (b) The contraction of the incoming arrows of ψ and $\overline{\psi}$ leaves an identity matrix on each outgoing index. In mathematical symbols, this is $\sum_{pld} \psi_{plrdu}\overline{\psi}_{pl\bar{r}d\bar{u}} = \delta_{r\bar{r}}\delta_{u\bar{u}}$.

site $\mathbf{x}$, which hosts n_p Majorana fermion modes (representing the physical degrees of freedom—$n_p = 2$ for the case of one complex fermion per site), one prepares a state ρ_ψ in the tensor product of the virtual Hilbert space and the physical Hilbert space on $\mathbf{x}$. Due to the assumed translation invariance, ρ_ψ is the same for all $\mathbf{x}$. A fermion TNS supported in the physical Hilbert space, with bond dimension $\chi = \sqrt{2}^{n_v}$ [56], is formed as the partial overlap between ρ_{virtual} and $\prod_{\mathbf{x}} \rho_\psi$:

$$\rho_{\text{TNS}} = \text{Tr}_{\text{virtual}}(\rho_{\text{virtual}} \prod_{\mathbf{x}} \rho_\psi), \tag{11}$$

where ρ_{virtual} is always Gaussian.

The TNS is a GfTNS when ρ_ψ is also Gaussian [25,26,28], i.e., one where the physical properties are entirely determined, via Wick's theorem, by a covariance matrix of the form of Eq. (7). From now on, we assume ρ_ψ to be Gaussian and denote its covariance matrix as

$$\Gamma_\psi = \begin{bmatrix} A & B \\ -B^T & D \end{bmatrix}, \tag{12}$$

where A is $n_p \times n_p$, B is $n_p \times 4n_v$, and D is $4n_v \times 4n_v$. Treating Γ as a matrix with indices μ and ν, the covariance matrix of the GfTNS can be obtained as [25,26,28]

$$\Gamma_{\text{TNS}}(\mathbf{k}) = A + B(D + \Gamma_{\text{virtual}}(\mathbf{k}))^{-1}B^T, \tag{13}$$

where $\Gamma_{\text{virtual}}(\mathbf{k})$ is the momentum-space covariance matrix of ρ_{virtual} and is equal to

$$\Gamma_{\text{virtual}}(\mathbf{k}) = \begin{bmatrix} 0 & \Gamma_1(\mathbf{k}) \\ -\Gamma_1(\mathbf{k})^\dagger & 0 \end{bmatrix}, \tag{14}$$

where $\Gamma_1(\mathbf{k}) = -(e^{-ik_x} I_{2n_v} \oplus e^{-ik_y} I_{2n_v})$, with I_{2n_v} being the $2n_v \times 2n_v$ identity matrix. In writing $\Gamma_{\text{virtual}}(\mathbf{k})$, we have ordered the virtual modes in the order of l, d, r, and u legs shown in Fig. 6.

C. Isometric constraints on GfTNS

As proved in Ref. [23], the isometric structure and the fermionic structure are compatible in a TNS, in the sense that if the fermionic TNS is made of isometric tensors, the norm of the many-body fermion wave function can still be computed efficiently despite of the fermionic structure. For our purpose, we will simply consider a local tensor that is isometric as in Fig. 6; this is the same isometric constraint obeyed by the black tensors in Fig. 1(a). In the context of the GfTNS, on each leg of ψ live a number of Majorana fermion modes. Figure 6 simply means that the reduced density matrix of the modes on the right and the up legs is proportional to the identity, and thus that the covariance matrix entries vanish; $i/2\text{Tr}(\rho_\psi[\gamma^\mu, \gamma^\nu]) \propto i/2\text{Tr}([\gamma^\mu, \gamma^\nu]) = 0$ for all γ^μ and γ^ν on the right and up legs.

The reverse statement is also true: if ρ_ψ is Gaussian, and the block of the covariance matrix according to certain tensor legs is zero, then the tensor must be isometric with those legs having outgoing isometric arrows. This follows from Wick's theorem: all higher-order correlators among the outgoing legs in ψ are equal to the Pfaffian of the corresponding submatrix of the covariance matrix of the outgoing legs, which is identically zero. The full set of correlators determines the reduced density matrix entirely, which is the identity matrix, implying isometry.

We order the Majorana fermions in the order of the legs of ψ: p, l, d, r, and u, and use n_p, n_l, n_d, n_r, and n_u to denote the number of Majorana modes on each leg. According to the above discussion, the covariance matrix of an isometric tensor will have a zero block if we regroup the blocks according to incoming and outgoing arrows. The covariance matrix of an isometric ρ_ψ would have the additional block structure

$$\Gamma_\psi = \begin{bmatrix} A & B \\ -B^T & D \end{bmatrix} = \begin{bmatrix} \mathcal{A} & \mathcal{B} \\ -\mathcal{B}^T & \mathcal{D} \end{bmatrix} = \begin{bmatrix} \mathcal{A} & \mathcal{B} \\ -\mathcal{B}^T & 0 \end{bmatrix}. \tag{15}$$

A, B, and D follow the grouping separating physical and virtual fermions as in Eq. (12), where A is of size $n_p \times n_p$ and B is of size $n_p \times (n_l + n_d + n_r + n_u)$. The $\mathcal{A}$, $\mathcal{B}$, and $\mathcal{D}$ follow the grouping separating incoming and outgoing indices, where $\mathcal{A}$ is of size $n_{\text{in}} \times n_{\text{in}}$, and $\mathcal{B}$ is of size $n_{\text{in}} \times n_{\text{out}}$ with incoming dimension $n_{\text{in}} = n_p + n_l + n_d$ and outgoing dimension $n_{\text{out}} = n_u + n_r$. The $\mathcal{D}$ is sub-block of D that vanishes due to isometric constraint.

To construct a uniform isoGfTNS as in Fig. 1(a), one simply uses a covariance matrix the sub-blocks of which corresponding to the right and up virtual legs are zero. To construct an alternating isoGfTNS, one uses a unit cell of two tensors (see Appendix A 1), with different outgoing isometric arrows as in Fig. 1(b), and the corresponding sub-block of the covariance matrices of ψ vanishing: for one site in the unit cell, the sub-block of the right and up virtual legs is zero; for the other site, the sub-block of the right and down virtual legs is zero.

1. Variational parametrization

In the following, we show how to parametrize Γ_ψ for the isoGfTNS. Note that there are two other constraints on Γ_ψ in addition to the isometric constraints. The first is that $\Gamma_\psi \Gamma_\psi^T = I$ due to the fact that ρ_ψ is a pure state. The second is that Γ_ψ is real antisymmetric [57]. The antisymmetry requirement simply means that $\mathcal{A}$ is real antisymmetric. The purity requirement is equivalent to

(I) $\mathcal{B}^T\mathcal{B} = I$
(II) $\mathcal{A}^T\mathcal{A} = I - \mathcal{B}\mathcal{B}^T$
(III) $\mathcal{A}\mathcal{B} = 0$

Condition I means that $\mathcal{B}$ is an isometric matrix. To unpack condition II, using the antisymmetry of $\mathcal{A}$, let us write (assuming that n_{in} is even)

$$\mathcal{A} = R \bigoplus_{i=1}^{n_{\text{in}}/2} \begin{bmatrix} 0 & s_i \\ -s_i & 0 \end{bmatrix} R^T, \quad s_i \geq 0, \tag{16}$$

where R is orthogonal. Then condition II becomes

$$\mathcal{A}^T\mathcal{A} = R \bigoplus_{i=1} \begin{bmatrix} s_i^2 & 0 \\ 0 & s_i^2 \end{bmatrix} R^T = I - \mathcal{B}\mathcal{B}^T = I - \text{Proj}_{\mathcal{B}}, \tag{17}$$

which is an orthogonal projection matrix where the rank is $n_{\text{in}} - \text{rank}(\mathcal{B}) = n_{\text{in}} - n_{\text{out}}$. It follows that $s_i = 1$ for $i \leq \text{rank}(\mathcal{A})/2$, and $s_i = 0$ for $i > \text{rank}(\mathcal{A})/2$, and that the column space of R spans the orthogonal subspace to the column space of $\mathcal{B}$. Condition III follows directly from II.

Thus, to parametrize Γ_ψ, we consider an orthogonal matrix Q of size $n_{\text{in}} \times n_{\text{in}}$ and take the first n_{out} columns to be $\mathcal{B}$ and the other $n_{\text{in}} - n_{\text{out}}$ columns to be R:

$$Q = [\mathcal{B} \,|\, R], \quad \mathcal{A} = R \bigoplus_{i=1}^{n_{\text{in}}/2} \begin{bmatrix} 0 & 1 \\ -1 & 0 \end{bmatrix} R^T. \tag{18}$$

At the end, we note that if there is an even number of sites in the lattice and Q is the same on all sites, one can always choose Q to be a special orthogonal matrix, i.e., $\det(Q) = 1$, for all tensors in the TNS. Suppose that a link in the lattice connects sites a and b. The GfTNS state does not change if one swaps the order of two modes on both sites. This permutes the columns and the rows of Γ_a and Γ_b accordingly, which results in a permutation only on the columns of Q, flipping the determinant of Q. The only invariant in such operations is the parity of the sum of the determinants of all the Qs. Following this, the determinant of the Q on every site can be converted to 1, if one has an even number of sites in the system. In the following, we will always use an even number of sites and use only special orthogonal Qs.

2. Gradient-based energy minimization

To find the ground state within the isometric GfTNS manifold, one directly works with Q and does Riemannian minimization of the total energy. Given the system Hamiltonian

$$H = \sum_{\mathbf{k}} \sum_{\mu\nu} \gamma^{\mu\dagger}(\mathbf{k}) h(\mathbf{k})_{\mu\nu} \gamma^{\nu}(\mathbf{k}), \tag{19}$$

the expectation value of H in a Gaussian state Γ_{TNS} is [29]

$$\langle H|H\rangle = \sum_k i\text{Tr}[h(\mathbf{k})\Gamma_{\text{TNS}}(\mathbf{k})] + \text{Tr}(h(\mathbf{k})), \tag{20}$$

where Γ_{TNS} is a function of Q via Eqs. (13), (15), and (18). In the following we will use the isoGfTNS to study the representability of isoTNSs. See Sec. A 4 for details of the numerical optimization.

D. Gaussian constraints on isoTNSs

Here, we comment that Gaussian constraints restrict isoTNSs more than general TNSs. This can be seen from a counting argument on the dimension of the TNS and isoTNS variational manifold. The dimension of the variational manifold of all TNSs of certain bond dimension χ is given by the dimension of the manifold of the tensor in the TNS minus the dimension of the manifold of the gauge freedom on the virtual bond of the TNS. For example, for a translationally invariant MPS of bond dimension $d \times \chi \times \chi$, where d is the dimension of the local Hilbert space, the MPS tensors form a $d\chi^2$-dimensional complex manifold. The gauge freedom on the virtual bonds are the $\chi \times \chi$ invertible matrices, which, as a manifold, has complex dimension χ^2. Thus,

$$\dim_{\mathbb{C}} \text{MPS} = (d-1)\chi^2. \tag{21}$$

For the isometric MPS, the tensors form a $(d\chi, \chi)$-Stiefel manifold, which has effective complex dimension $d\chi^2 - \chi^2/2$. The gauge freedom are the (χ, χ) unitary matrices, which have effective complex dimension $\chi^2/2$. Thus,

$$\dim_{\mathbb{C}} \text{isometric MPS} = (d-1)\chi^2 = \dim_{\mathbb{C}} \text{MPS}, \tag{22}$$

which makes sense because every MPS can be brought into canonical form without increasing the bond dimension.

For 2D general TNSs and isoTNSs, similarly, the dimensions are, respectively,

$$\dim_{\mathbb{C}} \text{TNS} = d\chi^4 - 2\chi^2, \tag{23}$$

$$\dim_{\mathbb{C}} \text{isoTNS} = \left(d - \frac{1}{2}\right)\chi^4 - \chi^2. \tag{24}$$

They clearly differ, but the difference is quite mild. To achieve the same variational dimension, when χ is large,

the bond dimension would scale as

$$\chi_{\text{isoTNS}} = \left(\frac{d}{d-\frac{1}{2}}\right)^{1/4} \chi_{\text{TNS}} \underset{d=2}{\approx} 1.07\chi_{\text{TNS}}. \tag{25}$$

For Gaussian TNSs with two physical Majorana modes and n virtual modes on each leg, the variational manifolds for general GfTNSs and isoGfTNSs are, respectively, $\text{SO}(4n+2)$ and $\text{SO}(2n+2)$, giving

$$\dim_{\mathbb{R}} \text{Gaussian TNS} = \frac{(4n+2)(4n+1)}{2}, \tag{26}$$

$$\dim_{\mathbb{R}} \text{Gaussian isoTNS} = \frac{(2n+2)(2n+1)}{2}. \tag{27}$$

Asympototically for large n, if Gaussian TNSs and Gaussian isoTNSs are to have the same variational dimension, then

$$n_{\text{isoTNS}} = 2n_{\text{TNS}} \rightarrow \chi_{\text{isoTNS}} = \chi_{\text{TNS}}^2, \tag{28}$$

which is a much worse scaling than Eq. (25). One thus expects that the Gaussian constraint restricts isoTNSs more than regular TNSs.

IV. NUMERICAL RESULTS

Using the framework and algorithms of noninteracting isoGfTNSs and interacting isoTNSs, we compare the performance of the uniform and alternating *Ansätze* on various paradigmatic systems, including (i) the stacked-chains example from Sec. II A, (ii) the Fermi surface, (iii) the band insulator, (iv) the $p_x + ip_y$ mean-field superconductor, and (v) the transverse-field Ising model. In each case, we find that the alt-iso(Gf)TNS outperforms the uni-iso(Gf)TNS, providing evidence that the alt-isoTNS has more representative power than the uni-isoTNS. Additionally, for the free-fermionic systems, we compare to the GfTNS, which has no isometric constraint, to demonstrate the loss in representability from imposing the isometric constraints necessary for quantum circuit equivalence.

A. Stacked chains

To test our argument of the entanglement structure in Sec. II A, we consider a collection of 1D free-fermion states hopping only along the $(1,1)$ diagonals or the $(1,-1)$ diagonals on a 2D square lattice. Using the isoGfTNS technique, the ground state is computed as both a uni-isoTNS and an alt-isoTNS. The energy result is presented in Fig. 7. We have also plotted the generic GfTNS result without any isometric constraints. We see that when the entanglement is only along the $(1,1)$ diagonals, the uni-isoTNS is actually as accurate as the unconstrained TNS and better than the alt-isoTNS. But when the entanglement is along the $(1,-1)$ direction, the uni-isoTNS performs poorly while the alt-isoTNS better approximates the exact results. Also, the performance of the alt-isoTNS is the same for both $(1,1)$ and $(1,-1)$ chains, indicating that the *Ansatz* is insensitive to the directionality of entanglement. This strongly supports our arguments laid out in Sec. II A.

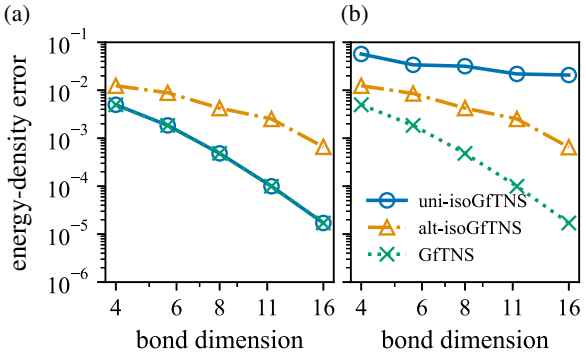


FIG. 7. The error in the ground-state energy for a 36×36 free-fermion system with hopping along the (a) $(1,1)$ or (b) $(1,-1)$ diagonals, using the GfTNS. While the isoTNS shows a strong dependence on the entanglement structure of the state, the alt-isoTNS is insensitive to this.

In practice for generic Hamiltonians, the states that one encounters will have entanglement along all directions, and thus we expect the alt-isoTNS to be a better *Ansatz* than the uni-isoTNS. We demonstrate this below for paradigmatic examples of noninteracting and interacting systems.

B. Fermi surface

Consider a 2D square lattice of free fermions with Hamiltonian:

$$H = -\sum_{\langle i,j\,|i,j\rangle} c_i^\dagger c_j, \tag{29}$$

where $c_i^\dagger$ and c_j are fermion creation and annihilation operators, and $\langle i,j\,|i,j\rangle$ denotes a pair of nearest-neighbor sites. This is a system of free fermions where the ground state has a Fermi surface. Systems with a Fermi surface are among the most challenging to represent as a tensor network state, because they are very strongly entangled; the entanglement entropy of a subregion with a boundary of size A scales as $A\log(A)$ [58,59], exceeding the conventional area law for ground states. We use this system as a benchmark to see the difference in the ability of the uni-isoTNS and the alt-isoTNS to represent strongly entangled systems.

We follow the setup in Ref. [29] which has studied the representability of generic, nonisometric TNS for the Fermi surface using the GfTNS. As in Ref. [29], we also study a system with an antiperiodic boundary in the x direction and a periodic boundary in the y direction, which

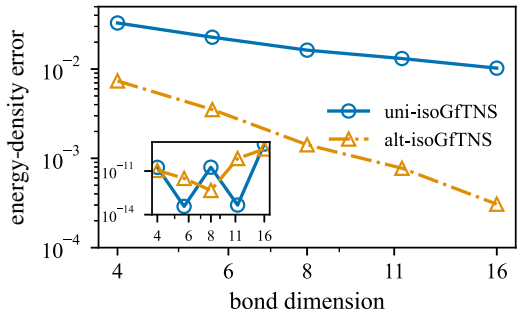


FIG. 8. The error in the ground-state energy for a 96×96 Fermi surface on a square lattice [see Eq. (29)]. The inset shows the norm of the energy gradient as a function of the bond dimension, indicating that our isoGfTNS numerics are well converged.

results in an open shell structure for the Fermi surface. We work directly in the momentum space. The isoTNS with these boundary conditions does not have an OHS, but we expect that the representability for large 2D systems is mainly limited by the isometries in the bulk. The calculation is performed for bond dimensions $\chi = \sqrt{2}^n, n = 4, 5, \ldots, 8$, for both the uni-isoTNS and the alt-isoTNS, of size 96×96, with isometric arrows drawn in Figs. 1(a) and 1(b) (excluding the OHS, i.e., the red tensors); as before, n is the number of pairs of Majorana Bell pairs used to represent each bond, which corresponds to $n/2$ complex fermion Bell pairs. As shown in Figs. 1(c) and 8, the alt-isoTNS captures the Fermi surface profoundly better than the uni-isoTNS. In particular, for the uni-isoTNS, there is an apparent directionality in the sharpness of the Fermi surface [60]. The entanglement perpendicular to the direction of the isometric arrows is much worse represented, as explained by the decoupled-chain argument in Sec. II A. The inset of Fig. 8 shows the norm of the energy gradient as a function of the bond dimension, which is a measure of how well converged our gradient-descent optimized isoGfTNS results are. The combination of initializing the gradient descent with 30–40 initial Gaussian states, the global nature of the gradient updates, and the small gradient norms together is an indication that we likely have found the true global minima.

C. Gapped free-fermion systems

We present additional evidence for the better representability of the alt-isoTNS for less entangled, gapped free-fermion systems. We study a topologically trivial band insulator with a finite band gap with the Hamiltonian

$$H_{\text{Insulator}} = -\sum_{\langle i,j|i,j\rangle} c_i^\dagger c_j + \sum_i \mu_i c_i^\dagger c_i, \tag{30}$$

where $\mu_i = 1$ on the even sublattice, and -1 on the odd sublattice. The ground-state and two-point correlator on a

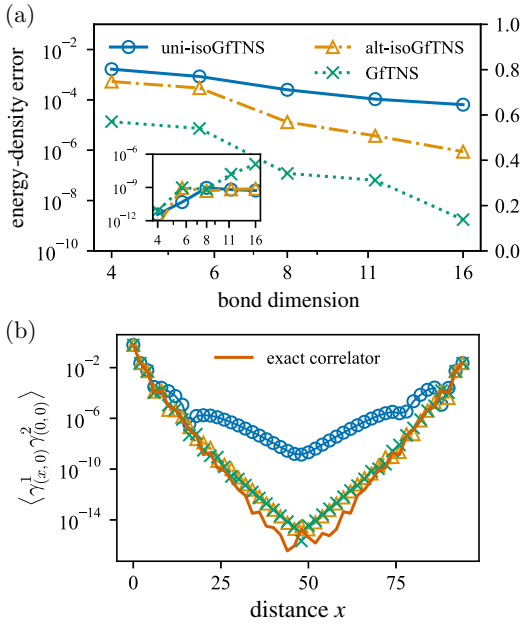


FIG. 9. The result of the GfTNS calculation for a 96×96 free-fermion insulator. (a) The error in the ground-state energy density. The inset shows the norm of the energy gradient as a function of the bond dimension. (b) The correlator $\left\langle \gamma^1_{(x,0)}\gamma^2_{(0,0)} \middle| \gamma^1_{(x,0)}\gamma^2_{(0,0)} \right\rangle$ along the x axis, as a function of the x distance. The bond dimension is 16.

96×96 lattice, with periodic boundary conditions along x and antiperiodic boundary conditions along y, are computed with the GfTNS, and the results are shown in Fig. 9. As seen, the alt-isoTNS also better approximates both properties of the insulator than the uni-isoTNS does with the same bond dimension. Although both the alt-isoTNS and the uni-isoTNS have a larger energy-density error than the unconstrained TNS, we see in Fig. 9(b) that the alt-isoTNS accurately captures long-distance two-point correlations in the state far better than the uni-isoTNS does.

D. $p_x + ip_y$ mean-field superconductor

The mean-field $p_x + ip_y$ superconductor (PipSC) has the following chiral Hamiltonian:

$$H_{\text{PipSC}} = -\sum_{\langle i,j|i,j\rangle} c_i^\dagger c_j + 2\sum_i c_i^\dagger c_i + \sum_{\langle i,j|i,j\rangle} (D_{ij} c_i c_j + \text{h.c.}), \tag{31}$$

where $D_{ij} = 1$ on the horizontal bonds and $\sqrt{-1}$ on the vertical bonds. If placed on a space manifold with no boundary, it has a finite energy gap and thus exponentially decaying correlators. PipSC, however, is topologically nontrivial, i.e., not in the same phase as a product state. It has been shown that the 2D GfTNS cannot be gapped, topologically nontrivial, *and* have a local parent

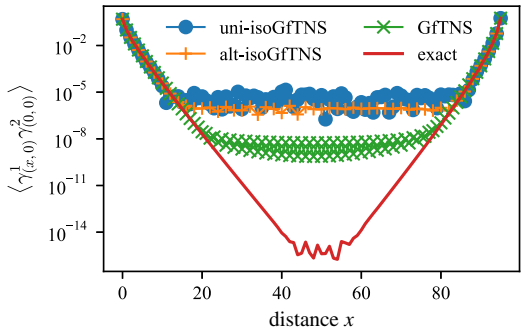


FIG. 10. The correlator $\left\langle \gamma^1_{(x,0)}\gamma^2_{(0,0)} \middle| \gamma^1_{(x,0)}\gamma^2_{(0,0)} \right\rangle$ along the x axis, as a function of the x distance on a 96×96 free-fermion $p_x + ip_y$ mean-field superconductor. The bond dimension is 16. The $\sim 10^{-15}$ error of the exact correlator is due to the floating-point error of the double precision that we have adopted in our numerical calculation.

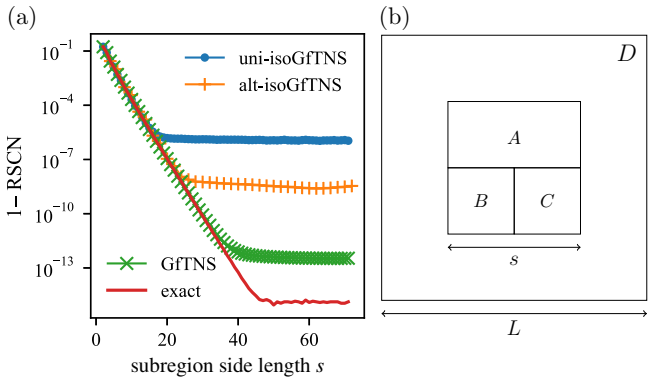


FIG. 11. (a) The real-space Chern number computed as a function of the subregion size. (b) The partitioning of the subregions. The GfTNS has bond dimension 16, and is on a 96×96 lattice.

Hamiltonian at the same time [26,27]. Here, we investigate the performance of the GfTNS in approximating the ground state of this chiral Hamiltonian. The ground state on a 96×96 lattice is computed with the GfTNS, and the results are shown in Fig. 10. As we see, there is a clear length scale for all three kinds of GfTNS beyond which the correlator stops decaying exponentially. This resembles the behavior of recent numerical studies of 2D TNS gapped chiral states using variational infinite projected entangled-pair states (PEPS), where the correlators decay exponentially for short distances and then eventually algebraically [61,62].

To access the "chirality" of the TNS, one can compute the real-space Chern number (RSCN) [63] of the optimized GfTNS. To compute the RSCN, one partitions the spatial region of a pure state into four regions A, B, C, and D such that A, B, and C form a triple joint and D complements ABC; see the configuration in Fig. 11. The RSCN in the Majorana basis is defined as

$$\nu = \frac{1}{16} 12\pi i [\mathrm{Tr}(PP_APP_BPP_C) - \mathrm{Tr}(PP_CPP_BPP_A)], \tag{32}$$

where $P_{ij} = \langle \gamma_j \gamma_i | \gamma_j \gamma_i \rangle$ is the Majorana correlator matrix. P_A, P_B, and P_C are the spatial projectors onto the corresponding regions, i.e., diagonal matrices with ith diagonal elements equal to 1 if site i is in the region, to 0 if not. Kitaev has proved that if the correlators decay exponentially, then as the size of all subregions goes to infinity, ν approaches an integer, and is proportional to the Hall conductance of the system [63]. As seen, the various types of GfTNS approximate well the exact Chern number of PipSC, which equals 1, but the error relative to the exact value saturates to a finite nonzero, albeit small, value. While the advantage of the alt-isoTNS is less pronounced in Fig. 10, we see that the alt-isoTNS captures the chirality of the state significantly better in Fig. 11.

It is, however, unlikely that the numerical optimization of a GfTNS can find a true gapless topologically nontrivial state, because such states are always noninjective [26], and hence have measure 0 in the variational manifold. Thus, the length scale in both the correlator and the RSCN is a result of the tension between good quantitative approximation of the chiral ground state and the general inability of the GfTNS to represent a gapped chiral state. The tensor network representation of chiral states deserves further study.

E. DMRG^2 study of 2D critical transverse-field Ising model

To compare the representing power of the uni-isoTNS and the alt-isoTNS for interacting spin systems, we use the DMRG^2 algorithm [21] to find the ground states using these two *Ansätze*. The DMRG^2 algorithm is essentially a nested loop over two levels of DMRG. We optimize each column sequentially, sweeping left to right and vice versa. Within each column, we find the ground state of the effective Hamiltonian of that column using traditional 1D DMRG. At a high level, DMRG^2 is analogous to the standard DMRG sweeping algorithm if we view each column as a site, now with each site being updated itself with DMRG. As we do the left-right sweep, we use MM to shift the orthogonality column to the column that we are optimizing. The isometric form provides stability to the DMRG^2 algorithm as in the 1D case. The algorithm is essentially the same for the alt-isoTNS and the uni-isoTNS, with the small change of MM mentioned in Sec. II D.

As a concrete example, we study the 2D transverse-field Ising (TFI) model at criticality on a square lattice with open

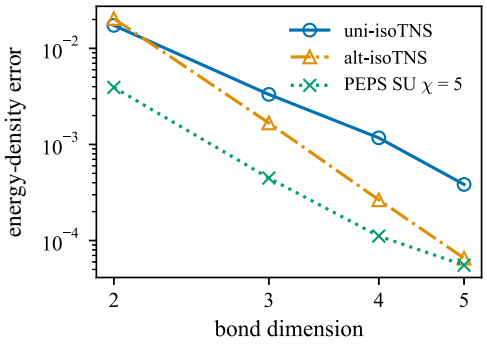


FIG. 12. The DMRG^2 results for the critical 2D transverse-field Ising model ($g = 3.04438$) on a 12×12 square lattice with open boundary conditions. The accuracy of the alt-isoTNS increases with the bond dimension faster than that of the uni-isoTNS. For the ground-truth energies, we use 1D DMRG on a $\chi = 2048$ MPS, which agrees within statistical error with the quantum Monte Carlo results. The PEPS simple-update results at the same bond dimensions are provided for comparison.

boundary conditions,

$$H = -\sum_{\langle ij \rangle} Z_i Z_j + g \sum_i X_i, \tag{33}$$

where $g = 3.04438$. We have chosen the system size to be 12×12 so that 1D snake DMRG with $\chi = 2048$ gives accurate ground-state energy, within a statistical error of 10^{-5} with quantum Monte Carlo with 3×10^9 cluster updates. For the 2D isoTNS, we set the bond dimension to be χ everywhere except on the orthogonality column (row), where we use a larger bond dimension χ^2. As shown in Fig. 12, for $\chi = 2, 3, 4, 5$, the energy density converges as a power law of the bond dimension. Interestingly, the power for the alt-isoTNS is considerably larger than the power for the uni-isoTNS. Moreover, for the uni-isoTNS, as we change the horizontal isometric arrows from leftward to rightward during the sweep, we need to change the vertical isometric arrows from upward to downward. Otherwise, the uni-isoTNS DMRG^2 does not converge. See Sec. >A 3 for details of isometric directions during the DMRG sweep. This result suggests that the alt-isoTNS does have an algorithmic advantage in finding the ground state of local isotropic Hamiltonians. While at this system size we do not see an advantage over 1D DMRG, we expect one to develop as $L_y \to \infty$. Using imaginary time TEBD2 to optimize the ground states of the critical TFI, an infinite-strip uni-isoTNS finds a lower energy (when compared to QMC) than infinite 1D DMRG when $L_y = 20$ [22].

To place the accuracy of the isoTNS results in context, we also present the PEPS simple-update (SU) [64] results for comparison [65]. As seen in Fig. 12, at bond dimension 5, the alt-isoTNS is comparable to PEPS SU, although slightly worse. We expect the more costly PEPS full update [66] to give more accurate results than SU. However, unconstrained PEPS still lacks the ability to be efficiently prepared on a quantum computer, which remains a key advantage of the isoTNS *Ansatz*.

V. DISCUSSION AND CONCLUSIONS

In this work, we have first introduced the alternating isoTNS *Ansatz*. Second, we have extended the GfTNS framework, a standard tool for efficiently investigating tensor network representability, to include isometric constraints, resulting in the the isoGfTNS *Ansatz*. Using a pedagogical example of stacked chains, we have argued that entanglement in the isoTNS is mediated along the isometric arrows, and thus, unlike the uni-isoTNSs, the alt-isoTNSs admit efficient paths to mediate entanglement both parallel and orthogonal to the isometric constraints in the network. As generic states are expected to have entanglement in all directions, we expect alt-isoTNSs to perform better than uni-isoTNSs, as we have demonstrated in a number of both noninteracting and interacting examples. Using the introduced isoGfTNS framework, we have demonstrated that alt-isoGfTNSs outperform uni-isoGfTNSs in representing the ground states of paradigmatic free-fermion systems, namely (1) decoupled stacks of chains, (2) the Fermi surface, (3) the gapped-band insulator, and (4) the $p_x + ip_y$ mean-field superconductor. We expect a similar advantage in the representation power for interacting alt-isoTNSs over fermionic uni-isoTNSs based on the argument that the limiting factor for the isoTNS is not interaction but entanglement [29]. Turning to the transverse-field Ising model, an interacting spin model, we have shown that the energy-density error of the alt-isoTNS converges with a larger power law than that of the uni-isoTNS. This indicates that, despite the two *Ansätze* having the same leading-order computational cost and retaining the same benefits of optimization in an orthonormal basis as compared to the generic TNS, the alt-isoTNS has an representation advantage over the uni-isoTNS. Finally, from a quantum circuit perspective, we have shown that the alt-isoTNS can be sequentially generated as a quantum circuit with a depth of $O(L^2)$ compared to $O(L)$ of the uni-isoTNS. The advantage of the alt-isoTNS over the uni-isoTNS implies that given the same number of local gates, different circuit depths and a different order of applying the gates significantly changes the result of state preparation on a quantum computer.

The alt-isoTNS, or more generally the nonuniform variation of isometric constraints on a TNS, opens up many interesting research directions. On the theoretical side, a key question is whether there are phases of matter that can be efficiently represented by the alt-isoTNS but not by the uni-isoTNS, or vice versa. While uni-isoTNSs have recently been shown to be able to represent critical states with algebraic correlations, arising from classical partition

functions viewed as quantum states [17], the representability of chiral states is more subtle. For example, in a related paper to appear, some of us show that uni-isoGfTNSs cannot represent *gapless* chiral free-fermion systems, even though general GfTNSs can [26,27]. In this context, an important relevant question is whether gapless chiral states admit alt-isoGfTNS representations.

On the practical side, due to the improved performance and negligible computational overhead, one should use the alt-isoTNS in place of the uni-isoTNS for many-body simulations. A generalization that could further improve the representability is to allow the vertical isometric arrows to alternate even more freely, i.e., not just alternate between each column. In such a "free-form" isoTNS, the optimization algorithm may automatically determine which pattern of vertical isometric arrow directions is the best for the particular system being simulated. For example, when sweeping across the columns left to right (and vice versa), one can choose the column arrow direction based on the MM error for the two-column splitting, i.e., one can always choose the direction giving the smaller error. Another promising direction is the optimization of the isoTNS with variational Monte Carlo (VMC). Due to its low computational complexity in bond dimension, variational Monte Carlo for tensor network states has recently become the state of the art in simulating a TNS ground state in 2D [67]. A key step in VMC algorithms is the sampling of basis states according to their Born probabilities. All uni-isoTNSs, alt-isoTNSs, and "free-form" isoTNSs can be more efficiently sampled than generic TNSs [68,69]; therefore it is natural to extend VMC to the isoTNS, where again the alt-isoTNS is expected to provide an improvement compared to the uni-isoTNS.

The variety of isometric constraints on TNSs can go beyond uniform, alternating, and free forms. Going one step further, one may consider networks composed of tensors that are isometric upon several different groupings of legs. One example is given in the recently proposed dual-isometric PEPS [70], which allow for efficient calculation of a broader class of observables than previously possible with conventional isoTNSs. The isoGfTNS approach that we have introduced here offers two distinct advantages:

(1) In general, each of the TNSs with different isometric constraints requires a specific optimization algorithm utilizing the isometric condition. For example, the algorithm for dual-isometric PEPS [70] is distinct from that for uni-isoTNSs. However, this is not the case in the framework of the GfTNS. One does not need to develop different optimization algorithms for different isometric constraints. GfTNSs with arbitrary isometric constraints can all be parametrized by simply demanding that sub-blocks of the correlation matrix corresponding to outgoing legs are zero, as discussed in Sec. III C, and optimized accordingly. This enables high-throughput evaluation of many different isometric constraints.

(2) In general, algorithms for TNSs with different isometric constraints, such as those discussed in Sec. II D and gradient-descent algorithms for dual-isometric PEPS, have a complexity polynomial in bond dimension. Our isoGfTNS algorithms have a huge advantage in that complexity scaling is polylogarithmic in bond dimension.

Together, this establishes the isoGfTNS as a tool of independent interest in studying the representability of the TNS *Ansätze* with various isometric constraints.

Although in this work we have focused on 2D systems on square lattices, a further interesting future direction is to investigate the effect of isometric constraints on TNS representation in higher dimension or different lattice geometry. The complexity of the GfTNS and the isoGfTNS scales much more favorably, only polynomially with dimension, making such a study possible.

Finally, due to the strong connection between isoTNSs and unitary circuits and the ability to efficiently optimize isoTNSs on classical computers, the study of various isometric networks will shed light on quantum state preparation on near-term quantum computers. In addition, the alt-isoTNS *Ansatz* finds potential applications in machine learning, particularly for scenarios where models are trained classically but inference is performed on quantum devices. Algorithms for manipulating classical isoTNSs can be interpreted as approximation algorithms for quantum circuit compilation. For example, one can imagine the approximation algorithm using MMs to transform an alt-isoTNS to a uni-isoTNS corresponds to a quantum circuit compilation of approximately transforming an $O(L^2)$-depth circuit into $O(L)$ depth. Looking forward, further exploration of isoTNSs may provide valuable insights into scalable quantum state preparation and the development of quantum assisted machine-learning applications.

ACKNOWLEDGMENTS

Y.W. is supported by a start-up grant from Institute of Physics Chinese Academy of Sciences (IOP-CAS). L.W. and Q.Y. are supported by the National Natural Science Foundation of China under Grants No. T2225018, No. 92270107, No. 12188101, and No. T2121001, and the Strategic Priority Research Program of the CAS under Grants No. XDB0500000 and No. XDB30000000. Z.D., S.A., and M.Z. were supported by the U.S. Department of Energy, Office of Science, Basic Energy Sciences, under Early Career Grand No. DE-SC0022716. S.L. and F.P. were supported by the Deutsche Forschungsgemeinschaft (DFG, German Research Foundation) TRR80. F.P. acknowledges

support from the DFG under Germany's Excellence Strategy–EXC–2111–390814868, TRR 360—492547816, and DFG Research Unit FOR 5522 (project-id 499180199), the European Research Council (ERC) under the European Union Horizon 2020 research and innovation program (Grant Agreement No. 771537), as well as the Munich Quantum Valley, which is supported by the Bavarian state government with funds from the Hightech Agenda Bayern Plus. Y.W. is grateful for discussions with Hong-Hao Tu. We are grateful to an anonymous referee for providing the PEPS simple-update data for comparison with the isoTNS interacting results.

DATA AVAILABILITY

The data that support the findings of this paper are openly available [71]; embargo periods may apply.

APPENDIX

1. GfTNS with unit cell

When there are unit cells in the system, let $\gamma_{\mathbf{r}}^{\mu}$ denote a Majorana fermion mode, where $\mathbf{r}$ denotes the unit-cell position, and μ collectively denotes all other intracell degrees of freedom such as the position within a unit cell and the first or the second part of a complex fermion mode. On each site $\mathbf{x}$, one still assigns a local Gaussian linear map with covariant matrix $A(\mathbf{x})$, and takes

$$A \equiv A(\mathbf{r}) = \bigoplus_{\mathbf{x}:\text{in unit cell } \mathbf{r}} A(\mathbf{x}), \tag{A1}$$

where translational invariance demands that $A(\mathbf{r})$ be the same for all $\mathbf{r}$. Let B and D be similarly defined. Then, the physical covariance matrix of the TNS is still given by Eq. (13).

2. Larger MERA for $|\searrow\rangle$

As discussed in Sec. II A, we can understand the representational difference between the alt- and uni-isoTNS by considering stacks of diagonal chains. For the negative diagonal state $|\searrow\rangle$, the uni-isoTNS most efficiently represents this state as a MERA. In Fig. 13, we demonstrate this for a single chain of length $L = 16$. For this larger system size than $L = 5$ shown in Fig. 3(c), we see the alternating layers of unitaries and isometries. If we were to stack the MERA for all possible $(1, -1)$ diagonal chains, we would

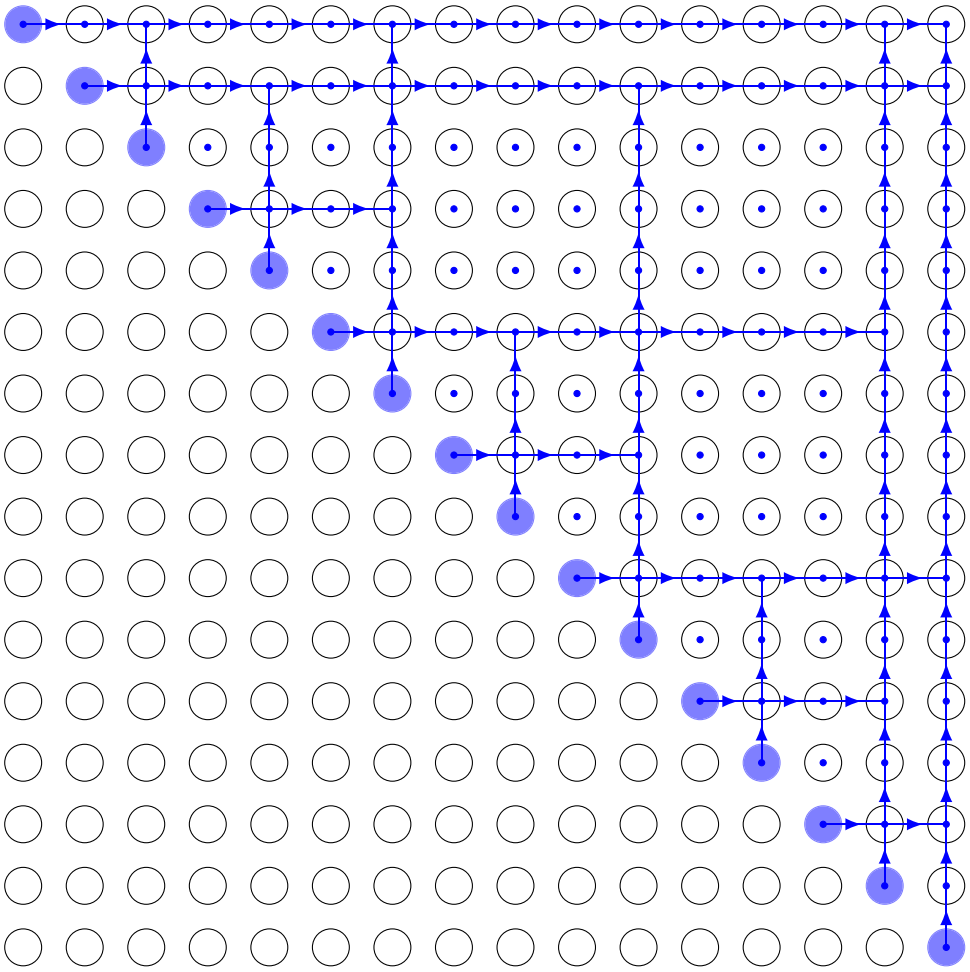


FIG. 13. The MERA representing a single $(1, -1)$ diagonal chain, embedded on a 16×16 square lattice.

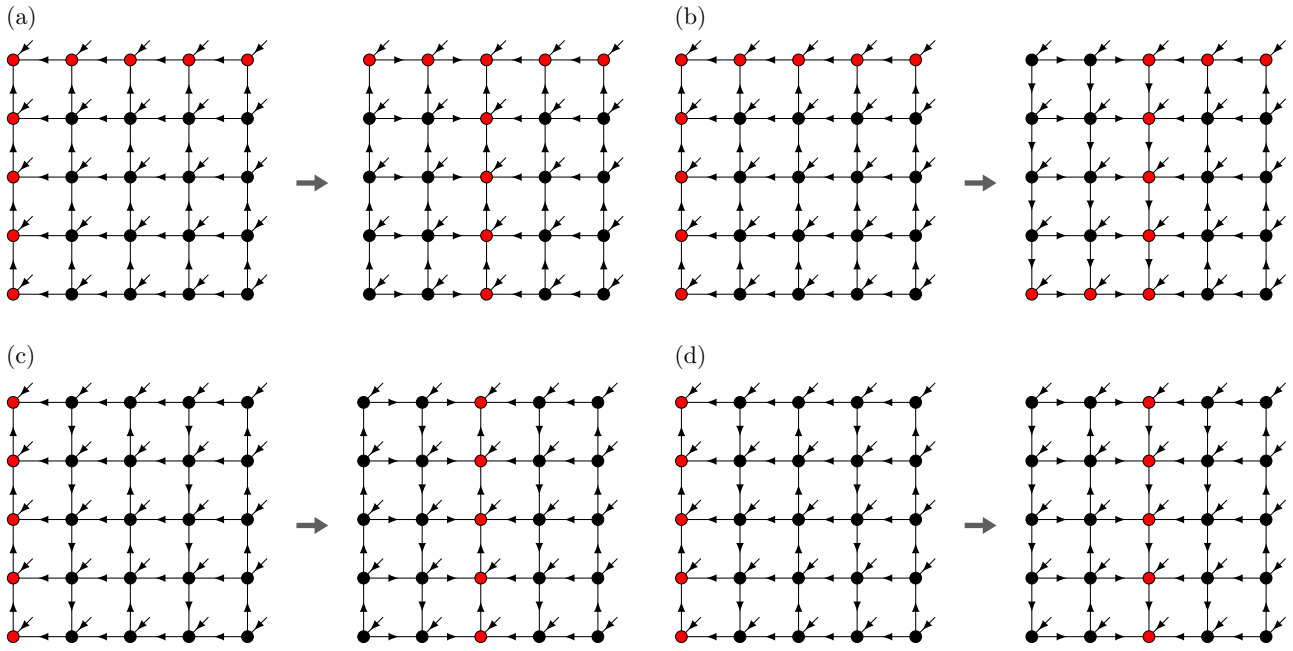


FIG. 14. The isometric directions as we move the orthogonality column from the left to the middle during a DMRG^2 sweep: (a) uni-isoTNS, ↑ to ↑ sweep; (b) uni-isoTNS, ↑ to ↓ sweep; (c) alt-isoTNS, ↑↓ to ↑↓ sweep; (d) alt-isoTNS, ↑↓ to ↓↑ sweep.

see that the tensor in the top-right corner, the OC, would require virtual bond dimensions of χ^{L-1}, where χ is the bond dimension of each MERA.

3. Isometric directions during a DMRG^2 sweep

In this appendix, we discuss different choices of isometric directions during a DMRG^2 sweep and how they change the result. As illustrated in Fig. 14, as we move the orthogonality column and optimize the tensors along the column, the horizontal arrows are required to point into the orthogonality column, but we can choose the direction of the vertical arrows. For uni-isoTNSs with isometry arrows originally pointing up and to the left, we can either keep the vertical arrows up during the sweep, namely an ↑ to ↑ sweep [Fig. 14(a)], or reverse the vertical arrows as we sweep, an ↑ to ↓ sweep [Fig. 14(b)]. Similarly, for alt-isoTNSs, we can choose between the ↑↓ to ↑↓ sweep [Fig. 14(c)] and the ↑↓ to ↓↑ sweep [Fig. 14(d)].

Since we have shown that the isometric direction affects the representing power, it is interesting to test how they change the result of DMRG^2 . In Fig. 15 we show the DMRG^2 result for the four different choices of isometric directions. Here, we plot the energy as a function of the sweep index. In each sweep, the orthogonality column is moved from left to the right and back again, so that a non-integer value is when the OHS is away from the left edge of the system. The ↑ to ↓ sweep for uni-isoTNSs and the two types of alt-isoTNS sweeps converge to stable oscillations, but the ↑ to ↑ sweep for uni-isoTNSs does not converge. This is most likely because the time direction, along which entanglement is mediated, constantly changes during the ↑ to ↑ sweep, while other choices do not suffer from this problem. The stable oscillation patterns indicate that the position of the orthogonality column also affects the representing power of the isoTNS. Finally, note that the energy is often minimized when the OHS is in the middle of the system (near sweep indices $n + \frac{1}{4}$ and $n + \frac{3}{4}$ for integer n

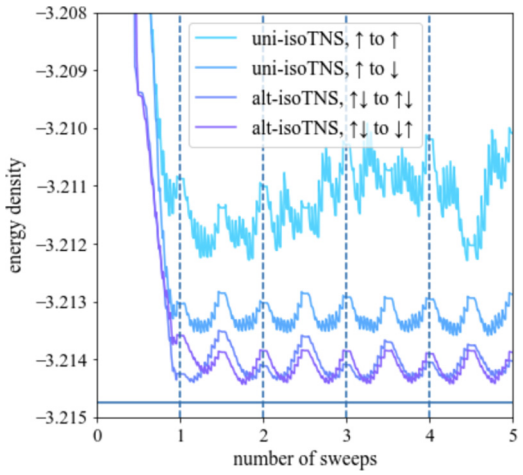


FIG. 15. The energy density during DMRG^2 sweeps of the critical TFI model on a 12 × 12 square lattice. Five full sweeps are shown in the figure. In each full sweep, the orthogonality column is moved from the left to the right and back to the left. The different colors indicate different vertical isometric directions during the sweep. The bond dimension of the isoTNS is 4, and the bond dimension along the orthogonality column is 16.

as the OHS will be in the middle of the 2D system), as this minimizes the average distance of most tensors from the OHS. Finally, note that the energy is often minimized when the OHS is in the middle of the system (near sweep indices $n + \frac{1}{4}$ and $n + \frac{3}{4}$ for integer n as the OHS will be in the middle of the 2D system), as this minimizes the average distance of most tensors from the OHS.

4. Optimization details for GfTNS

We also comment on how the GfTNS numerical optimization is done in practice. The optimization is nonconvex. To overcome this, one can seed the simulation with different initial states. In our case, 30–40 different random initial states have each been independently optimized for 10 000 iterations, and then the one with the lowest energy has been picked to be further optimized for 100 000 iterations. Every 10 000 iterations, we have also added some randomness to the state to escape local minima. Then after that, if the gradient is still large, we have used Newton's method to do a final descent. After these steps, the energy gradients of the optimized states can often go below 10^{-9}. The optimization is done on a GPU, and the computation is parallelized over the different **k**-points of the translationally invariant systems.

[1] F. Verstraete and J. I. Cirac, Renormalization algorithms for quantum-many body systems in two and higher dimensions, ArXiv:cond-mat/0407066.

[2] H. Niggemann, A. Klümper, and J. Zittartz, Quantum phase transition in spin-3/2 systems on the hexagonal lattice—optimum ground state approach, Z. Phys. B Condens. Matter **104**, 103 (1997).

[3] T. Nishino and K. Okunishi, A density matrix algorithm for 3D classical models, J. Phys. Soc. Jpn. **67**, 3066 (1998).

[4] G. Sierra, in *Proceedings of the Workshop on the Exact Renormalization Group* (World Scientific, Faro, Portugal, 1998).

[5] S.-J. Ran, E. Tirrito, C. Peng, X. Chen, L. Tagliacozzo, G. Su, and M. Lewenstein, *Tensor Network Contractions: Methods and Applications to Quantum Many-Body Systems* (Springer Nature, 2020).

[6] J. I. Cirac, D. Pérez-García, N. Schuch, and F. Verstraete, Matrix product states and projected entangled pair states: Concepts, symmetries, theorems, Rev. Mod. Phys. **93**, 045003 (2021).

[7] M. C. Bañuls, Tensor network algorithms: A route map, Annu. Rev. Condens. Matter Phys. **14**, 173 (2023).

[8] J. Naumann, E. L. Weerda, M. Rizzi, J. Eisert, and P. Schmoll, An introduction to infinite projected entangled-pair state methods for variational ground state simulations using automatic differentiation, SciPost Phys. Lect. Notes **86** (2024).

[9] S. R. White, Density matrix formulation for quantum renormalization groups, Phys. Rev. Lett. **69**, 2863 (1992).

[10] U. Schollwöck, The density-matrix renormalization group, Rev. Mod. Phys. **77**, 259 (2005).

[11] G. Vidal, Efficient classical simulation of slightly entangled quantum computations, Phys. Rev. Lett. **91**, 147902 (2003).

[12] J. Haegeman, C. Lubich, I. Oseledets, B. Vandereycken, and F. Verstraete, Unifying time evolution and optimization with matrix product states, Phys. Rev. B **94**, 165116 (2016).

[13] M. P. Zaletel and F. Pollmann, Isometric tensor network states in two dimensions, Phys. Rev. Lett. **124**, 037201 (2020).

[14] R. Haghshenas, M. J. O'Rourke, and G. Kin-Lic Chan, Conversion of projected entangled pair states into a canonical form, Phys. Rev. B **100**, 054404 (2019).

[15] K. Hyatt and E. M. Stoudenmire, DMRG approach to optimizing two-dimensional tensor networks, ArXiv:1908.08833.

[16] C. Schön, E. Solano, F. Verstraete, J. I. Cirac, and M. M. Wolf, Sequential generation of entangled multiqubit states, Phys. Rev. Lett. **95**, 110503 (2005).

[17] Y.-J. Liu, K. Shtengel, and F. Pollmann, Simulating two-dimensional topological quantum phase transitions on a digital quantum computer, Phys. Rev. Research **6**, 043256 (2024).

[18] X. Chen, A. Dua, M. Hermele, D. T. Stephen, N. Tantivasadakarn, R. Vanhove, and J.-Y. Zhao, Sequential quantum circuits as maps between gapped phases, Phys. Rev. B **109**, 075116 (2024).

[19] X. Chen, M. Hermele, and D. T. Stephen, Sequential adiabatic generation of chiral topological states, ArXiv:2402.03433.

[20] H.-K. Zhang, S. Liu and S.-X. Zhang, Absence of Barren Plateaus in finite local-depth circuits with long-range entanglement, Phys. Rev. Lett. **132**, 150603 (2024).

[21] S.-H. Lin, M. P. Zaletel, and F. Pollmann, Efficient simulation of dynamics in two-dimensional quantum spin systems with isometric tensor networks, Phys. Rev. B **106**, 245102 (2022).

[22] Y. Wu, S. Anand, S.-H. Lin, F. Pollmann, and M. P. Zaletel, Two-dimensional isometric tensor networks on an infinite strip, Phys. Rev. B **107**, 245118 (2023).

[23] Z. Dai, Y. Wu, T. Wang, and M. P. Zaletel, Fermionic isometric tensor network states in two dimensions, Phys. Rev. Lett. **134**, 026502 (2025).

[24] W. Kadow, F. Pollmann, and M. Knap, Isometric tensor network representations of two-dimensional thermal states, Phys. Rev. B **107**, 205106 (2023).

[25] C. V. Kraus, N. Schuch, F. Verstraete, and J. I. Cirac, Fermionic projected entangled pair states, Phys. Rev. A **81**, 052338 (2010).

[26] T. B. Wahl, H.-H. Tu, N. Schuch, and J. I. Cirac, Projected entangled-pair states can describe chiral topological states, Phys. Rev. Lett. **111**, 236805 (2013).

[27] J. Dubail and N. Read, Tensor network trial states for chiral topological phases in two dimensions and a no-go theorem in any dimension, Phys. Rev. B **92**, 205307 (2015).

[28] Q. Yang, X.-Y. Zhang, H.-J. Liao, H.-H. Tu, and L. Wang, Projected *d*-wave superconducting state: A fermionic projected entangled pair state study, Phys. Rev. B **107**, 125128 (2023).

[29] Q. Mortier, N. Schuch, F. Verstraete, and J. Haegeman, Tensor networks can resolve Fermi surfaces, Phys. Rev. Lett. **129**, 206401 (2022).

[30] R. Masaoka, S. Ono, H. C. Po, and H. Watanabe, Frustration-free free fermions and beyond, ArXiv:2503.12879.

[31] Z.-Y. Wei, D. Malz, and J. I. Cirac, Sequential generation of projected entangled-pair states, Phys. Rev. Lett. **128**, 010607 (2022).

[32] F. Pollmann, S. Mukerjee, A. M. Turner, and J. E. Moore, Theory of finite-entanglement scaling at one-dimensional quantum critical points, Phys. Rev. Lett. **102**, 255701 (2009).

[33] N. Bao, C. Cao, S. M. Carroll, A. Chatwin-Davies, N. Hunter-Jones, J. Pollack, and G. N. Remmen, Consistency conditions for an AdS multiscale entanglement renormalization ansatz correspondence, Phys. Rev. D **91**, 125036 (2015).

[34] C. Schön, K. Hammerer, M. M. Wolf, J. I. Cirac, and E. Solano, Sequential generation of matrix-product states in cavity QED, Phys. Rev. A **75**, 032311 (2007).

[35] M.-C. Banuls, D. Pérez-García, M. M. Wolf, F. Verstraete, and J. I. Cirac, Sequentially generated states for the study of two-dimensional systems, Phys. Rev. A **77**, 052306 (2008).

[36] Z.-Y. Wei, D. Malz, A. González-Tudela, and J. I. Cirac, Generation of photonic matrix product states with Rydberg atomic arrays, Phys. Rev. Res. **3**, 023021 (2021).

[37] M. Foss-Feig, D. Hayes, J. M. Dreiling, C. Figgatt, J. P. Gaebler, S. A. Moses, J. M. Pino, and A. C. Potter, Holographic quantum algorithms for simulating correlated spin systems, Phys. Rev. Res. **3**, 033002 (2021).

[38] S. Anand, J. Hauschild, Y. Zhang, A. C. Potter, and M. P. Zaletel, Holographic quantum simulation of entanglement renormalization circuits, PRX Quantum **4**, 030334 (2023).

[39] R. Haghshenas, E. Chertkov, M. DeCross, T. M. Gatterman, J. A. Gerber, K. Gilmore, D. Gresh, N. Hewitt, C. V. Horst, M. Matheny, T. Mengle, B. Neyenhuis, D. Hayes, and M. Foss-Feig, Probing critical states of matter on a digital quantum computer, Phys. Rev. Lett. **133**, 266502 (2024).

[40] L. Slattery and B. K. Clark, Quantum circuits for two-dimensional isometric tensor networks, ArXiv:2108.02792.

[41] Due to the isometry conditions on each tensor, with physical dimension $d = 2$ one cannot have a nontrivial uniform bond dimension $\chi > 1$ for all virtual legs at the boundary. As shown in Figs. 5(a) and 5(b), the vertical bond dimensions of the leftmost column (i.e., furthest from the OC) are trivial. Thus, tensors in the final column, when viewed as a gates of the resulting quantum circuit, can be applied in parallel with other gates. This is a boundary effect. For the alt-isoTNS, only one unitary gate can be applied at each time step inside the bulk. Therefore, the depth of an alt-isoTNS circuit is $\mathcal{O}(L_x \cdot L_y)$.

[42] I. H. Kim, Holographic quantum simulation, ArXiv:1702.02093.

[43] Y. Du, T. Huang, S. You, M.-H. Hsieh, and D. Tao, Quantum circuit architecture search for variational quantum algorithms, npj Quantum Inf. **8**, 62 (2022).

[44] Y. Du, Z. Tu, X. Yuan, and D. Tao, Efficient measure for the expressivity of variational quantum algorithms, Phys. Rev. Lett. **128**, 080506 (2022).

[45] L. Funcke, T. Hartung, K. Jansen, S. Kühn, and P. Stornati, Dimensional expressivity analysis of parametric quantum circuits, Quantum **5**, 422 (2021).

[46] Y. Wu, J. Yao, P. Zhang, and H. Zhai, Expressivity of quantum neural networks, Phys. Rev. Res. **3**, L032049 (2021).

[47] T. Haug, K. Bharti, and M.S. Kim, Capacity and quantum geometry of parametrized quantum circuits, PRX Quantum **2**, 040309 (2021).

[48] Q. Miao and T. Barthel, Isometric tensor network optimization for extensive Hamiltonians is free of barren plateaus, Phys. Rev. A **109**, L050402 (2024).

[49] T. Barthel and Q. Miao, Absence of barren plateaus and scaling of gradients in the energy optimization of isometric tensor network states, Commun. Math. Phys. **406**, 86 (2025).

[50] M. A. Levin and X.-G. Wen, String-net condensation: A physical mechanism for topological phases, Phys. Rev. B **71**, 045110 (2005).

[51] I. H. Kim and D. Ranard, Classifying 2D topological phases: Mapping ground states to string-nets, ArXiv:2405.17379.

[52] T. Soejima, K. Siva, N. Bultinck, S. Chatterjee, F. Pollmann, and M. P. Zaletel, Isometric tensor network representation of string-net liquids, Phys. Rev. B **101**, 085117 (2020).

[53] A. Kitaev, Fault-tolerant quantum computation by anyons, Ann. Phys. (NY) **303**, 2 (2003).

[54] N. Schuch, I. Cirac, and D. Pérez-García, PEPS as ground states: Degeneracy and topology, Ann. Phys. (NY) **325**, 2153 (2010).

[55] The left-regular matrix representation of a group G is defined as follows. Consider the vector space spanned by all group elements: $V = \text{span}\{g|g \in G\}$, where all gs are defined to be linearly independent. The matrix representation $\phi(g)$ of g in V is a permutation matrix the action of which is defined on the basis of V as $\phi(g)\,|g'\rangle = |gg'\rangle \forall g' \in G$. This is clearly a, possibly reducible, matrix representation of G, because $\phi(g)\phi(g') = \phi(gg')$. All $\phi(g)$ are traceless expect when $g = e$.

[56] When n_v is even, a GfTNS can be constructed as a conventional TNS with bond dimension $2^{n_v/2}$. When n_v is odd, this is no longer possible, yet the odd-n_v GfTNS is still well defined. Thus, one should take $\chi = \sqrt{2}^{n_v}$ as a continuation from even n_v to odd n_v.

[57] S. Bravyi, Lagrangian representation for fermionic linear optics, Quantum Inf. Comput. **5**, 216 (2005).

[58] D. Gioev and I. Klich, Entanglement entropy of fermions in any dimension and the Widom conjecture, Phys. Rev. Lett. **96**, 100503 (2006).

[59] B. Swingle, Entanglement entropy and the Fermi surface, Phys. Rev. Lett. **105**, 050502 (2010).

[60] From basic solid state physics, the directionality in the k-space translates into the same directionality in the real space.

[61] J. Hasik, M. Van Damme, D. Poilblanc, and L. Vanderstraeten, Simulating chiral spin liquids with projected entangled-pair states, Phys. Rev. Lett. **129**, 177201 (2022).
[62] E. L. Weerda and M. Rizzi, Fractional quantum Hall states with variational projected entangled-pair states: A study of the bosonic Harper-Hofstadter model, Phys. Rev. B **109**, L241117 (2024).
[63] A. Kitaev, Anyons in an exactly solved model and beyond, Ann. Phys. **321**, 2 (2006), January Special Issue.
[64] H. C. Jiang, Z. Y. Weng, and T. Xiang, Accurate determination of tensor network state of quantum lattice models in two dimensions, Phys. Rev. Lett. **101**, 090603 (2008).
[65] The PEPS SU data have been provided by an anonymous referee, to whom we are grateful.
[66] M. Lubasch, J. I. Cirac, and M.-C. Bañuls, Algorithms for finite projected entangled pair states, Phys. Rev. B **90**, 064425 (2014).
[67] W.-Y. Liu, Y.-Z. Huang, S.-S. Gong, and Z.-C. Gu, Accurate simulation for finite projected entangled pair states in two dimensions, Phys. Rev. B **103**, 235155 (2021).
[68] T. Vieijra, J. Haegeman, F. Verstraete, and L. Vanderstraeten, Direct sampling of projected entangled-pair states, Phys. Rev. B **104**, 235141 (2021).
[69] S. Anand, S. Thanvantri, Y. Wu, and M. P. Zaletel, Perfect sampling of isometric tensor networks and applications to finite temperature thermodynamics (to be published).
[70] X.-H. Yu, J. I. Cirac, P. Kos, and G. Styliaris, Dual-isometric projected entangled pair states, Phys. Rev. Lett. **133**, 190401 (2024).
[71] Y. Wu, Z. Dai, S. Anand, S.-H. Lin, Q. Yang, L. Wang, F. Pollmann, and M. Zaletel, GitHub data repository, https://github.com/yantaow/open_data/tree/main/wu2025alternating, 2025.